NAVAL POSTGRADUATE SCHOOL
Monterey, California

THESIS

STUDY OF CAVITATION AND FAILURE MECHANISMS OF SUPERPLASTIC 5083 ALUMINUM ALLOY

by

Juanito F. Boydon, Jr.

September 2003

Thesis Advisor: Terry R. McNelley

Approved for public release; distribution is unlimited

THIS PAGE LEFT INTENTIONALLY BLANK

REPORT DOCUMENTATION PAGE			*Form Approved OMB No. 0704-0188*
Public reporting burden for this collection of information is estimated to average 1 hour per response, including the time for reviewing instruction, searching existing data sources, gathering and maintaining the data needed, and completing and reviewing the collection of information. Send comments regarding this burden estimate or any other aspect of this collection of information, including suggestions for reducing this burden, to Washington headquarters Services, Directorate for Information Operations and Reports, 1215 Jefferson Davis Highway, Suite 1204, Arlington, VA 22202-4302, and to the Office of Management and Budget, Paperwork Reduction Project (0704-0188) Washington DC 20503.			
1. AGENCY USE ONLY *(Leave blank)*	**2. REPORT DATE** September 2003	**3. REPORT TYPE AND DATES COVERED** Master's Thesis	
4. TITLE AND SUBTITLE: Study of Cavitation and Failure Mechanisms of a Superplastic 5083 Aluminum Alloy			**5. FUNDING NUMBERS**
6. AUTHOR(S) Boydon, Juanito F.			
7. PERFORMING ORGANIZATION NAME(S) AND ADDRESS(ES) Naval Postgraduate School Monterey, CA 93943-5000			**8. PERFORMING ORGANIZATION REPORT NUMBER**
9. SPONSORING / MONITORING AGENCY NAME(S) AND ADDRESS(ES) General Motors Corp., Research and Development Center, Warren, MI (Dr. Paul E. Krajewski, Technical Program Monitor), under subcontract with Univ.of Texas-Austin (Prof. Eric Taleff)			**10. SPONSORING / MONITORING AGENCY REPORT NUMBER**
11. SUPPLEMENTARY NOTES The views expressed in this thesis are those of the author and do not reflect the official policy or position of the Department of Defense or the U.S. Government.			
12a. DISTRIBUTION / AVAILABILITY STATEMENT Approved for public release; distribution is unlimited		**12b. DISTRIBUTION CODE**	

13.   ABSTRACT *(maximum 200 words)*

Superplastic forming of AA5083 is an economical way to create components of complex shape while retaining the high strength and stiffness-to-weight ratios associated with aluminum alloys. However, failure of the material due to formation and linkage of cavities during superplastic deformation poses a major obstacle in effective industrial employment of this technology. Deformed samples of AA5083 were analyzed by various techniques after superplastic deformation under uniaxial tension, biaxial tension, or plane strain conditions. The goal was to determine the roles of $MnAl_6$ second phase particles and the grain boundary disorientations in the processes of cavity formation and growth. Scanning electron microscopy (SEM) techniques included backscatter imaging (BSI), energy dispersive spectrometry (EDS) and orientation imaging microscopy (OIM) to identify and evaluate sites of cavity formation in these samples. Results of this study show that cavities form due to grain boundary sliding (GBS) and separation of boundaries. Second phase particles such as $MnAl_6$ were apparent on some separating boundaries but not on others. Cavities also grow from pre-existing voids introduced during prior processing. The role of GBS was confirmed by evaluating the grain-to-grain disorientations across newly formed small cavities. Results show that these disorientations are $\geq 7°$, a value consistent with the threshold value of disorientation for GBS in pure Aluminum.

14. SUBJECT TERMS Orientation Imaging Microscopy, Energy Dispersive X-ray Analysis, Superplasticity, Cavitation, Grain Boundary Sliding, Dislocation Creep.			**15. NUMBER OF PAGES** 87
			16. PRICE CODE
17. SECURITY CLASSIFICATION OF REPORT Unclassified	**18. SECURITY CLASSIFICATION OF THIS PAGE** Unclassified	**19. SECURITY CLASSIFICATION OF ABSTRACT** Unclassified	**20. LIMITATION OF ABSTRACT** UL

THIS PAGE LEFT INTENTIONALLY BLANK

**STUDY OF CAVITATION AND FAILURE MECHANISMS OF A
SUPERPLASTIC 5083 ALUMINUM ALLOY**

Juanito F. Boydon, Jr.
Lieutenant, United States Navy
Undergraduate (B.S.), United States Naval Academy, 1996

Submitted in partial fulfillment of the
requirements for the degree of

MASTER OF SCIENCE IN MECHANICAL ENGINEERING

from the

**NAVAL POSTGRADUATE SCHOOL
September 2003**

Author: Juanito F. Boydon, Jr.

Approved by: Terry R. McNelley
                          Thesis Advisor

                          Prof. Anthony J. Healey
                          Chairman, Department of Mechanical Engineering

THIS PAGE LEFT INTENTIONALLY BLANK

ABSTRACT

Superplastic forming of AA5083 is an economical way to create components of complex shape while retaining the high strength and stiffness-to-weight ratios associated with aluminum alloys. However, failure of the material due to formation and linkage of cavities during superplastic deformation poses a major obstacle in effective industrial employment of this technology. Deformed samples of AA5083 were analyzed by various techniques after superplastic deformation under uniaxial tension, biaxial tension, or plane strain conditions. The goal was to determine the roles of $MnAl_6$ second phase particles and the grain boundary disorientations in the processes of cavity formation and growth. Scanning electron microscopy (SEM) techniques included backscatter imaging (BSI), energy dispersive spectrometry (EDS) and orientation imaging microscopy (OIM) to identify and evaluate sites of cavity formation in these samples. Results of this study show that cavities form due to grain boundary sliding (GBS) and separation of boundaries. Second phase particles such as $MnAl_6$ were apparent on some separating boundaries but not on others. Cavities also grow from pre-existing voids introduced during prior processing. The role of GBS was confirmed by evaluating the grain-to-grain disorientations across newly formed small cavities. Results show that these disorientations are $\geq 7°$, a value consistent with the threshold value of disorientation for GBS in pure Aluminum.

THIS PAGE LEFT INTENTIONALLY BLANK

TABLE OF CONTENTS

THIS PAGE LEFT INTENTIONALLY BLANK

LIST OF FIGURES

THIS PAGE LEFT INTENTIONALLY BLANK

LIST OF TABLES

THIS PAGE LEFT INTENTIONALLY BLANK

ACKNOWLEDGEMENTS

THIS PAGE LEFT INTENTIONALLY BLANK

I.   INTRODUCTION

Superplastic forming has become an important industrial process in the manufacturing of metal parts of complex shape. The large tensile elongations and low flow stresses that are characteristic of superplasticity permit the use of gas-pressure forming to produce such shapes. In general, superplastic forming is accomplished at high temperatures and low strain rates and by applying differential gas pressure to a preheated alloy sheet to causes it to deform into a die and achieve a desired shape. Figure 1 illustrates this process. In contrast, the most common means of shaping sheet materials is by stamping with mated steel dies. Conventional stamping requires the steel dies to be much harder than the material being formed. Furthermore, the dies must endure the constant and high-energy impact of high-rate forming and so conventional stamping involves high initial investment that must be amortized over large production runs. Superplastic forming involves lower initial investment but lower production rates. This may not be a drawback for aerospace applications but may be important in other areas such as automotive.

In the automotive industry, an ongoing need to reduce vehicle weight and improve fuel efficiency has led to considerable interest in replacing steel with aluminum in sheet metal and other body parts.   The need for a high level of corrosion resistance restricts the range of possible aluminum alloys, although aluminum-magnesium alloys are particularly well suited for such applications. A typical Al-Mg commercial alloy is AA5083, which is widely used as a structural material in applications that require corrosion resistance and moderate strength and which has potential as an automotive body-sheet alloy. Conventional stamping of AA5083 into sheet metal parts is limited by the alloy's lower formability as compared to drawing-quality steels. Therefore superplastic of AA5083 and similar alloys is of considerable interest. [Ref. 1]

Although superplastic forming of aluminum alloys has the potential to provide intricate and lightweight components at competitive production costs it also has its

1

drawbacks. During forming of a sheet material by differential gas pressure under superplastic conditions, the sheet thins non-uniformly, becoming thinner in regions of large strain. As a result, areas of reduced strength and potential failure are created. Furthermore, the formation and linkage of internal cavities, i.e., cavitation, ultimately results in failure of the material during superplastic straining. Cavitation typically begins at small strains and progresses during straining, and so the volume fraction of cavities will tend to be largest in regions that are thinnest, further increasing the likelihood local failure of the material. Since cavitation is the primary culprit for this phenomenon isolating the mechanisms of cavitation will aid in bringing the superplastic forming of aluminum alloys one step closer to being used on a mass production scale. However, the mechanisms of cavitation are not fully understood and it is has been the subject of ongoing investigations. [Ref. 4, 7-10, 19-25]

The current study is a continuation of research on cavitation in this laboratory on AA5083 alloys [Maesta's thesis] that were designated as 978083 and 978901. Here, a material designated 978931 was also included in the investigation. In prior investigations these three materials exhibited varying tensile ductility despite essentially identical compositions, processing histories and initial grain sizes. Among these three materials the superplastic elongations of the 978901 material were consistently the lowest, those of the 978083 were intermediate while those of the 978931 were highest. Selected samples from 978083, 978901, and 978931 that had been deformed to failure under uniaxial tension were evaluated to determine assess the cavitation and failure mode. Energy-dispersive x-ray (EDX) analysis was combined with backscatter imaging (BSI) and employed to identify sites where cavities had formed and to determine, if any, the role of second phase particles, specifically $MnAl_6$, in the formation of cavities. Orientation Imaging Microscopy (OIM) was then implemented on the same regions examined using EDX / BSI to determine the nature of the grain-to-grain disorientations associated with these cavities. This combined microcopy technique was also used to analyze cavities in AA5083 materials that were formed under biaxial tension [material designation 978931(I)], and under plane strain conditions [material designation PS 978931(K)].
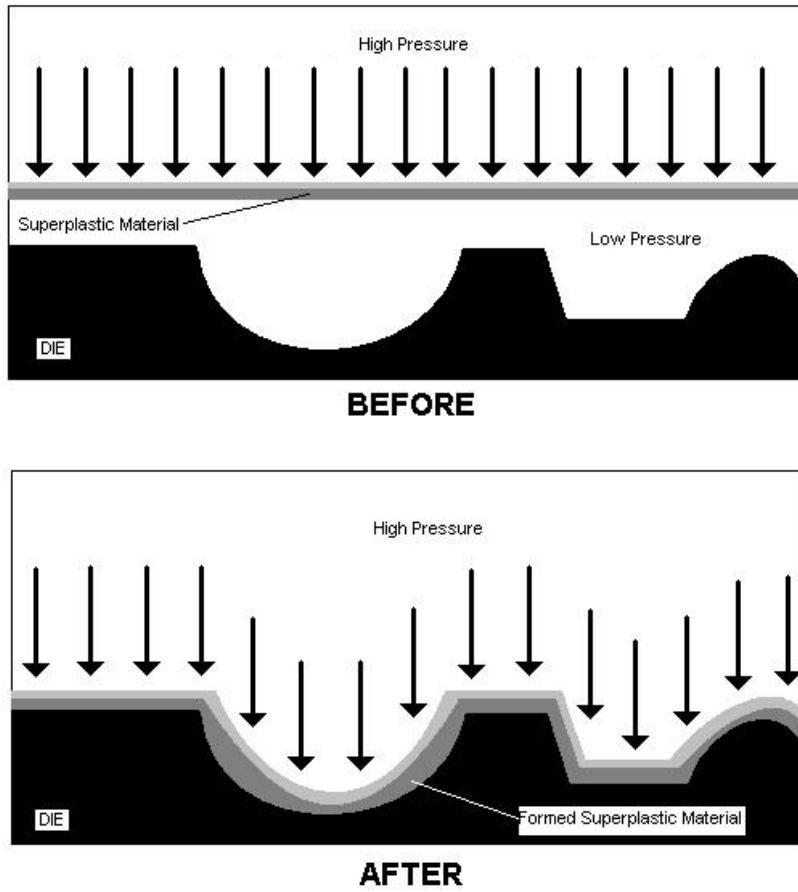
Figure 1. Schematic of superplastic forming process.

PAGE LEFT INTENTIONALLY BLANK

II.   BACKGROUND

A.   FINE-STRUCTURE SUPERPLASTICITY (FSS)

Superplasticity is defined as "the ability of a polycrystalline material to exhibit, in a generally isotropic manner, very high tensile elongations prior to failure." [Ref. 2] Superplasticity has been reported in a broad range of metallic and ceramic materials. Superplastic materials typically exhibit large values of strain-rate sensitivity coefficient, *m*, during deformation at an elevated temperature. Following Hertzberg, the flow stress-- strain-rate relation can be expressed as

$$\sigma = \frac{F}{A} = K\dot{\varepsilon}^m \quad \text{Equation 2.1}$$

where σ is flow stress, F is the applied force, A is the cross-sectional area, K is a material constant, and $\dot{\varepsilon}$ is the true strain rate [Ref. 3]. Values of m > 0.33 are typical in superplastic materials, whereas ordinary metals and alloys have values of m < 0.2. On the other hand, m approaches unity for material such as hot glass during tensile deformation.

Materials displaying superplastic qualities attain tensile elongations $\geq$ 150%. In fine-grained metallic materials, for example, tensile elongations of thousands of percent have been documented. In 1992, Higashi achieved an elongation of 8000% in a Cu-Al alloy. [Ref. 2] This type of superplastic behavior is referred to as fine-structured superplasticity (FSS). In order to develop FSS in metal-based materials, four essential requirements must be met. These are 1) fine grain size, 2) presence of second phase particles, 3) high angle boundaries and 4) equiaxed grain shapes.

Grain sizes for superplastic metals are typically 10 μm or less, and such fine grain sizes provide two advantages in FSS materials. The first advantage is that as grain size decreases the strain rate increases when grain boundary sliding (GBS) is the dominant deformation mechanism. Further discussion of the GBS deformation mechanism will be provided in the next section. The strain rate is normally related to grain size as

$$\dot{\varepsilon} \propto d^{-(2\ or\ 3)} \quad \text{Equation 2.2}$$

where d is the grain size. [Ref. 2] The grain size exponent of -2 refers to lattice diffusion control of GBS, while an exponent of -3 refers to grain boundary diffusion control of GBS. The second advantage of having a fine grain structure is that it reduces the flow stress in the material, which, in turn, reduces the applied forces during superplastic forming.

The presence of fine second phase particles that are uniformly distributed throughout the material inhibits grain growth during the superplastic forming process. This inhibition maintains the fine grain size within the material. Second phase particles, however, may contribute to the failure of the material during the forming process by serving as nucleation sites for cavities and/or preventing the occurrence of GBS. This study will examine the role of second phase particles, in particular $MnAl_6$, in the formation cavities in AA5083 samples.

The third requirement is that grain boundaries must be high energy (i.e., high angle, or disordered). This reduces the sliding resistance of the boundaries. The final requirement is that the shapes of the grains must be equiaxed. This allows the grain boundaries to experience shear stresses that are necessary for GBS to occur. [Ref. 2] In addition to the four requirements, the grain boundaries should be mobile and resistant to tensile separation. During GBS, mobile grain boundaries reduces the stress concentration at the triple points and thus preventing cavities from forming. Furthermore, grain boundaries should not be prone to ready tensile separation.

## B.	SUPERPLASTIC DEFORMATION MECHANISMS

This thesis is concerned with superplasticity in AA5083 alloys. Extensive research has been conducted into the deformation behavior and mechanisms of this material, mainly through tensile tests at strain rates from $3 \times 10^{-4}\ s^{-1}$ to $3 \times 10^{-2}\ s^{-1}$ and at constant temperatures ranging from 425 °C to 500 °C. Changes in m-values were

observed during these tests. At low strain rates, $m \sim 0.5$, while the m-value decreased to about 0.2 at high strain rates; this was attributed to a linear combination of two independent deformation mechanisms contributing to the combined elevated temperature deformation of the material. [Ref. 4, 5].

As mentioned in the previous section, the first independently operating deformation mechanism is grain boundary sliding (GBS) accommodated by slip processes, particularly near triple junctions. GBS occurs in a mantle-like region within and adjacent to the grain boundaries. The value of $m = 0.5$ is characteristic of plastic deformation by GBS. This mechanism usually dominates at low strain rates and high temperatures, typically above approximately 0.5 of the homologous temperature, i.e. $\frac{T}{T_m} \geq 0.5$, where T_m is the absolute melting point of the solid.

The second independently operating deformation mechanism is dislocation creep (with $m = 0.2 - 0.33$). Dislocation creep refers to deformation that is controlled by slip in the lattice within the grain. The slip process involves both glide on slip planes and climb over physical obstacles. The overall rate for dislocation creep can be expressed as:

$$\frac{1}{\dot{\varepsilon}_t} = \frac{1}{\dot{\varepsilon}_g} = \frac{1}{\dot{\varepsilon}_c} \qquad \text{Equation 2.3}$$

where $\dot{\varepsilon}_t$, $\dot{\varepsilon}_g$ and $\dot{\varepsilon}_c$ represent the overall creep strain rate, the dislocation glide strain rate and the climb strain rate, respectively, for dislocation creep. [Ref. 2] In this relationship, the mechanism having the slower strain rate will be rate controlling. The range in m values for dislocation creep reflects the rate and temperature dependence of the dislocation glide and climb rates.

For independent contributions from GBS and dislocation creep, the overall strain rate, $\dot{\varepsilon}$, may be assumed to be given by

$$\dot{\varepsilon} = \dot{\varepsilon}_{DIS} + \dot{\varepsilon}_{GBS} \qquad \text{Equation 2.4}$$

where $\dot{\varepsilon}_{GBS}$ is the strain rate due to GBS. There are various models that have been proposed to describe each of these independent deformation mechanisms. These models generally assume that each mechanism may be described separately by a relationship similar to that of equation 2.1, however, the appropriate values of *K* and *m* for the individual terms are assigned based on the deformation mechanism itself. Furthermore, such models generally incorporate temperature through diffusion coefficients. Such models may be combined to yield [Ref 2, 4, 6]

$$\frac{\dot{\varepsilon}}{D_L} = \frac{10^{11}}{b^2}\left(\frac{\sigma}{E}\right)^5 + \frac{2\times10^9}{\overline{L}^2}\left(\frac{\sigma}{E}\right)^2 \qquad \text{Equation 2.5}$$

where D_L is lattice diffusivity, b is the Burger's vector, $\overline{L}$ is the mean linear intercept grain size, and E is the modulus of elasticity. The first term on the right is the contribution of climb-controlled dislocation creep, which is independent of grain size. The stress exponent of 5 in this term is the reciprocal of the strain rate sensitivity coefficient; thus, $m = 0.2$ if this term dominates. The second term on the right describes GBS, which is grain-size dependent. The stress exponent of 2 equates to $m = 0.5$ and superplastic ductility when this term dominates. Examination of Equation 2.5 reveals that reducing the mean linear intercept grain size, $\overline{L}$, increases the contribution of the second term on the right hand side of Equation 2.5. In turn, this results in an increased range of strain rate, $\dot{\varepsilon}$, over which GBS predominates and wherein $m \cong 0.5$. Thus grain size refinement enhances the range of dominance of the superplastic mechanisms.

C.   CAVITATION MECHANISMS

While the various deformation mechanisms associated with superplasticity have been identified, the failure mechanisms, including cavity nucleation and linkage, have not been fully characterized. With respect to superplastic materials, cavities are voids originating from the grain boundaries that have gone through stages of nucleation and subsequent growth. As growth continues, linkage of these voids leads to eventual failure of the alloy during forming or testing. While pre-existing voids are often present in rolled alloys due to fracture or decohesion of constituent particles, it is generally believed

that voids are nucleated during deformation by a number of possible mechanisms. [Ref. 7] As seen in Figure 2, possible mechanisms include intersection of intragranular slip with non-deformable second phase particles and grain boundaries; sliding of grains along grain boundaries (GBS) which is not fully accommodated by diffusional transport into these regions; and vacancy condensation on grain boundaries. [Ref. 8]

In this study, non-deformable second phase particles, of nominal composition MnAl$_6$, are deemed the second-phase particles most likely to be associated with cavity formation. As mentioned in Section A, second phase particles may prevent grain growth and help maintain a fine grain size. However, cavitation can also occur at the matrix/second phase interfaces, because the interfaces act as stress concentration sites where heterogeneous deformation takes place. Research on the superplasticity of Al-Mg-Mn conducted by Taleff suggested that particulates observed in transmission electron microscopy (TEM) studies are most likely MnAl$_6$ and can serve as nucleation sites for cavities. [Ref. 9] Further microscopy techniques will be used to investigate this observation.
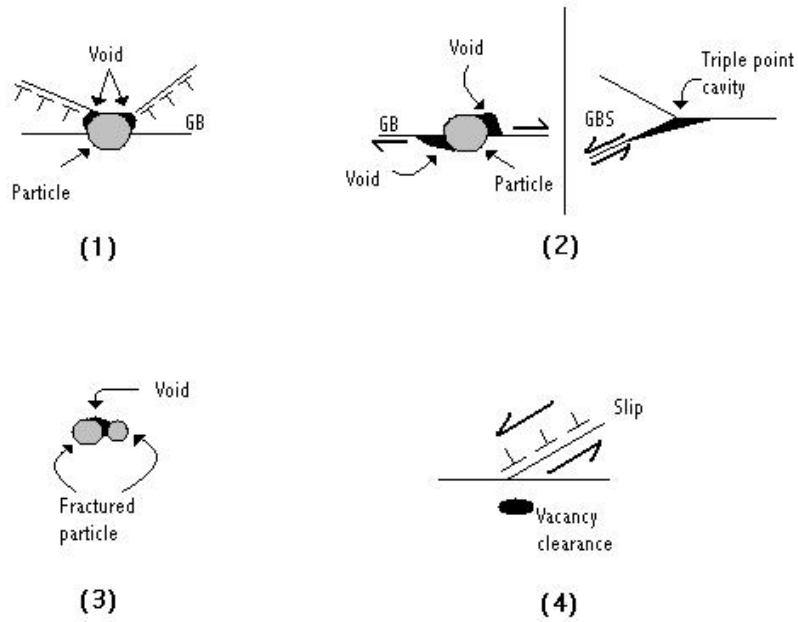
Figure 2. Illustration of possible cavitation mechanisms. 1. Interagranular slip intersection with non-deformable second phase particles and grain boundaries. 2. Sliding of grains along grain boundaries (GBS) which could not be fully accommodated by diffusional transport into these regions. 3. Fragmented particles in a microstructure containing coarse intermetallics. 4. Vacancy condensation on grain boundaries. (After: Ref. 8)

D. SUMMARY OF PREVIOUS WORK

Prior to the current research, a preliminary study of cavitation was carried out on four AA5083 samples, designated 978901(A20), 978083(A25), 978901(A17) and 978083(A24). Mechanical test data and microstructural observations are summarized in Table 1. The study conducted by Maestas suggested that the low ductility values correlated with the number fraction of cavities that had formed, and the boundaries with higher disorientations are the type of boundaries most likely to form a cavity.

Material Designation	Deformation Temp. (°C)	Strain Rate (s^{-1})	% Elongation to Failure (ε_f)	Cavity Fraction Number	Q
978901(A20)	450 °C	3 X 10^{-4}	178.5	0.01715	4.3
978083(A25)	450 °C	3 X 10^{-4}	203.5	0.00635	11.7
978901(A17)	500 °C	3 X 10^{-4}	183	0.04104	
978083(A24)	500 °C	3 X 10^{-4}	205	0.01348	

Table 1. The Mechanical testing data for selected materials investigated for cavitation behavior. (From: Ref. 4)

In Table 1, the values of a quantitative necking parameter, Q, suggested that cavitation had played a role in the premature failure of these materials [Ref. 4]. This value Q is the normalized difference between q and q^*, and is defined as follows,

$$Q = \left(\frac{q - q^*}{q^*}\right) \times 100\% . \qquad \text{Equation 2.6}$$

The parameter, q , is the degree of neck development at fracture. It is determined from the width, w , and the thickness, t , at the failure location of the sample; q is defined as follows, where A_0 is the cross-sectional area of the undeformed sample and $A = w^* t$ [Ref. 10]:

$$q = \frac{A_0 - A}{A_0}.$$ Equation 2.7

The parameter, $q*$, is the theoretical reduction-in-area for a neck-free sample having the same elongation-to failure, e_f, as that measured for a tested sample; $q*$ is defined as follows,

$$q* = \left(1 - \frac{1}{1 + e_f}\right) \times 100\%.$$ Equation 2.8

According to Taleff and Kulas, having such a quantitative description of necking is beneficial since the mode of failure for the AA5083 materials is generally a combination of necking and cavitation. [Ref. 10].

From the Q values, the extent of cavitation is expected to differ among these materials. An OIM analysis was conducted to identify the onset of cavitation in these materials and attempt to characterize the extent of cavity formation and the nature of the boundaries that had developed cavities. A step-down procedure was used for all samples to identify the onset of cavitation. In the step-down procedure, 100 μm^2 areas of the sample were scanned starting near the midpoint of the test sample until the failure region was reached. Figure 3 demonstrates how this was accomplished for the 978083(A24) sample. Due to its low image quality relative to adjacent material, cavities appeared darker and were easily identified using grayscale maps.

Furthermore, the cavities were counted using the highlighting feature in the OIM analysis software. A histogram was generated for each 100 μm^2 area of the number fraction of points in the area as a function of image quality with the number of bins determined by Sturgis' Rule. [Ref. 11] The highlight feature was utilized to select, by bin, the area in the image quality grayscale map that corresponded, (in image quality), to that bin. When all the cavities were highlighted in the image quality grayscale map, the number fraction of all areas corresponding to cavities was summed resulting in the number fraction of points in the grayscale map that corresponded to cavities. This essentially resulted in an area fraction of cavities since a point in all the image quality

grayscale maps are identical in area. This same procedure was repeated at each area selected for analysis stepping down the gage section until the failure site was reached. [Ref. 4] Table 1 summarizes the cavity number fraction for all samples that were scanned.

The data revealed that the samples with the lower ductility {978901 (A17) & 978901 (A20)} had a higher number fraction of cavities, approximately 3 times greater than the samples with the higher ductility {978083(A24) & 978083(A25)}. Due to identical grain sizes and other features of these samples, this correlation suggested that there is a direct relationship between the area fraction of cavities and the ductility of the sample. [Ref. 4]

Further study was conducted on the nature of the boundaries that had sustained cavity formation. This was done using a feature of the OIM analysis software that identified the disorientation angle between any two points on a grain map. The analysis of the 978901(A17) material resulted in 101 different disorientations associated with cavities. A histogram showing the distribution of the range of disorientations by number is shown in Figure 4, for this material. The data shows cavity formation for disorientation angles $\geq 7°$. The data for the 978083(A24) material is also shown in Figure 4 as a distribution histogram. The data set for this material is half that of the 978901(A17) material ($50 = N$) due to the smaller number fraction of cavities present in this material. However, this data suggests that boundaries with disorientations $\gtrapprox 10°$ are the type of boundaries most likely to develop a cavity. [Ref. 4]

The shape of the distribution in Figure 4 is similar to the Mackenzie distribution above about 10°. Since the distribution in the annealed, undeformed condition was essentially the Mackenzie random distribution, it can be concluded that boundaries above about 10° disorientation have a probability of separation in approximate proportion to the relative number of such boundaries in the microstructure. [Ref. 4]

13
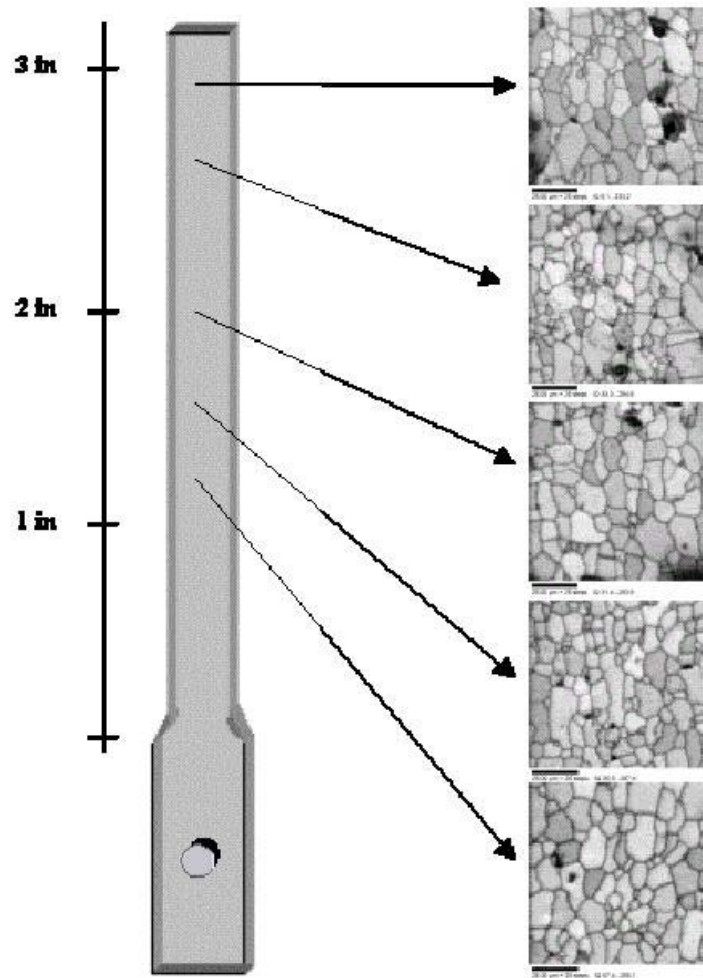
Figure 3. An illustration of the method used to "step down" the gage section of the sample. The image quality grayscale maps are from the material designated 978083(A24), deformed at 500 ºC and are typical of all the data taken for the other materials. The relative locations, examined by the OIM system, are similar on the other samples. (From: Ref. 4)
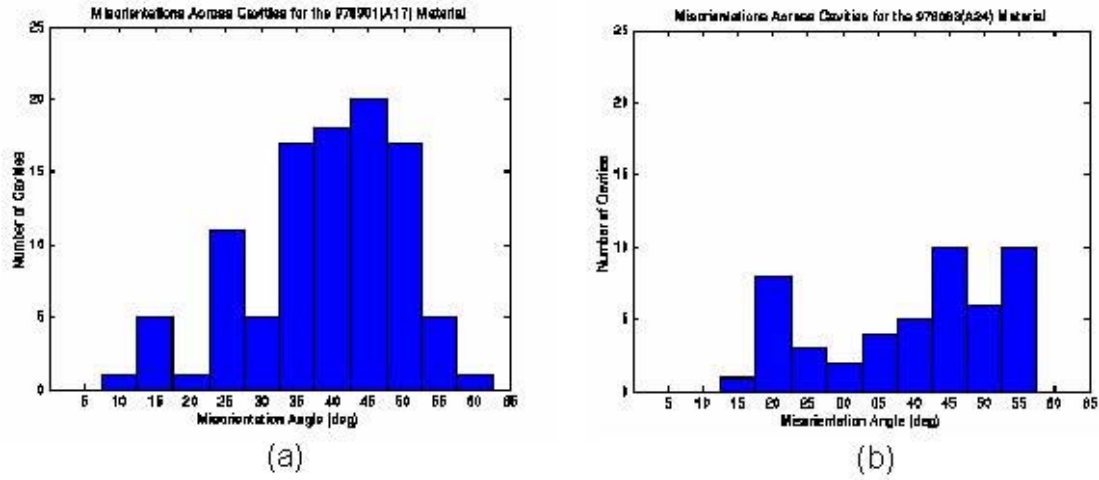
Figure 4. a) Histogram showing the distribution of cavities as a function of disorientation angle for the 978901(A17) material deformed at 500 ºC. b) Histogram showing the distribution of cavities as a function of disorientation angle for the 978083(A24) material deformed at 500 ºC. Note the data set is smaller due to the smaller number fraction of cavities. (After: Ref. 4)

THIS PAGE LEFT INTENTIONALLY BLANK

III. EXPERIMENTAL PROCEDURES

A. OVERVIEW

In this investigation, AA5083 aluminum-magnesium alloys that had been processed for grain refinement and superplasticity were examined. Specifically, this study looked at AA5083 materials designated 978083, 978901 and 978931, which had been provided by the University of Texas at Austin.

Energy dispersive x-ray analysis, backscatter imaging and OIM analysis were utilized in this study. These characterization tools were used in combination to 1) identify cavitation sites; 2) identify second phase particles, such as $MnAl_6$, and their association with cavity formation; 3) identify the onset of cavitation and determine its role in the failure of these materials during elevated temperature deformation.

B. MATERIALS

University of Texas provided samples from 978083, 978901 and 978931 which had been deformed under tensile test conditions corresponding to superplastic forming conditions. In addition, 978931 samples that were superplastically formed under biaxial tension and plane strain conditions were also provided for analysis. The compositions (in wt. pct.) of the materials are provided in Table 2 and from the table it is evident that the 978083 material generally contains a higher content of each alloying element.

Lot No.	Si	Fe	Cu	Mn	Mg	Cr	Zn	Ti	Zr
978083	0.09	0.21	0.04	0.86	4.71	0.01	0.05	0.01	0.00
978901	0.06	0.11	0.01	0.78	4.69	0.06	0.00	0.01	0.00
978901	0.15	0.20	0.03	0.76	4.50	0.07	0.02	0.01	0.00

Table 2. Chemical composition data for 978083, 978901, and 978931 materials.

C.   SAMPLE SECTIONING

The tensile test samples were sectioned from the deformed tensile sample using a Buehler low-speed saw equipped with a diamond-wafering blade (Series 15 LC Diamond). The sectioning was conducted at a blade speed of 400 rpm with no more than 100 g load applied throughout the sectioning process. The samples were sectioned parallel to the rolling direction (RD) to facilitate examination of the effects of rolling in the rolling direction-normal direction (RD-ND) plane as illustrated in Figure 5.   The transverse direction (TD) plane underwent mechanical polishing, electro-polishing, and microscopy analysis to examine the microstructure of the deformed region.
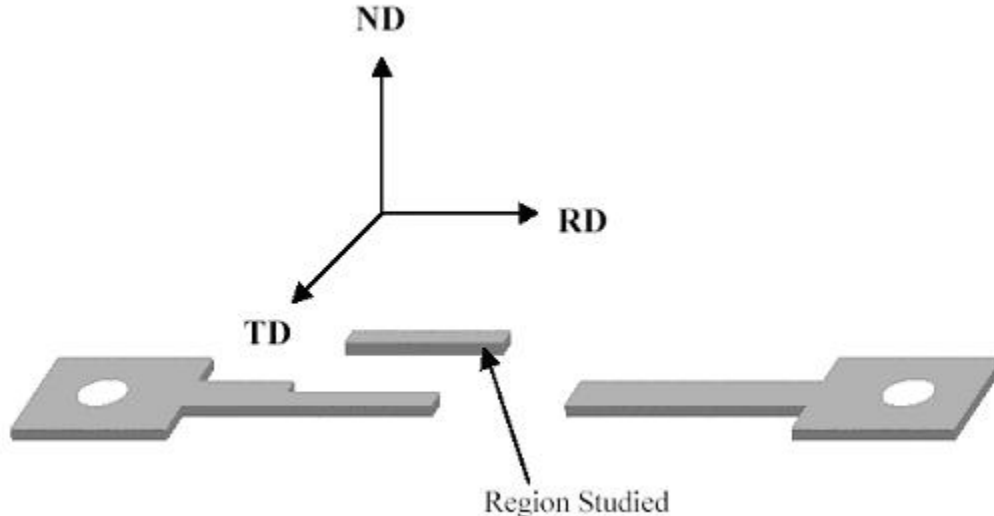
Figure 5. Schematic of a deformed tensile sample illustrating sectioning for OIM examination. (From: Ref.5).

Biaxial deformation occurs in a sheet sample formed into a hemispherical dome. Such a sample was also sectioned using the low speed saw. Figure 6 shows how the sample was cut for examination. Plane strain conditions exist in a sheet sample formed into an elongated dome. Due to the odd shape of the plane strain sample, shears were first used to cut around the desired areas. The low speed saw was then used to remove the

18

excess material around the segments. Figure 7 shows the deformed plane strain sample and where it was sectioned for examination.
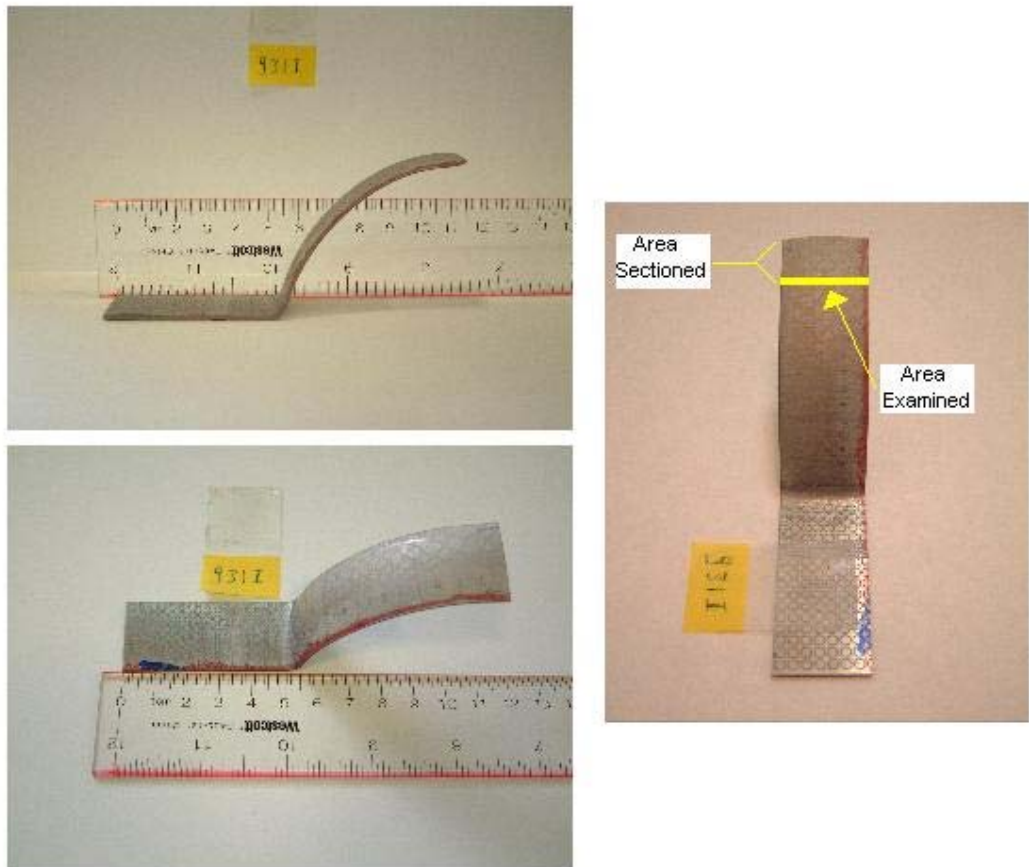
Figure 6. Pictures of 978931(I), biaxial tension test sample. The picture on the right shows where the sample was sectioned and examined.
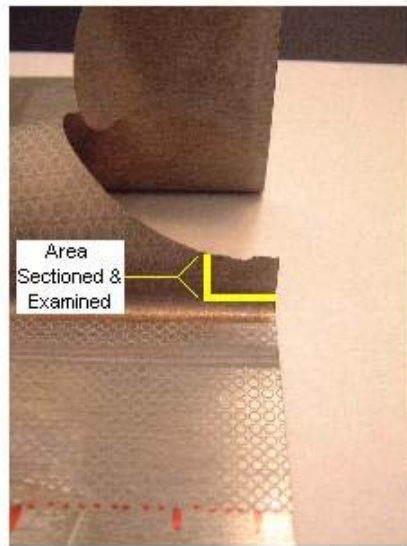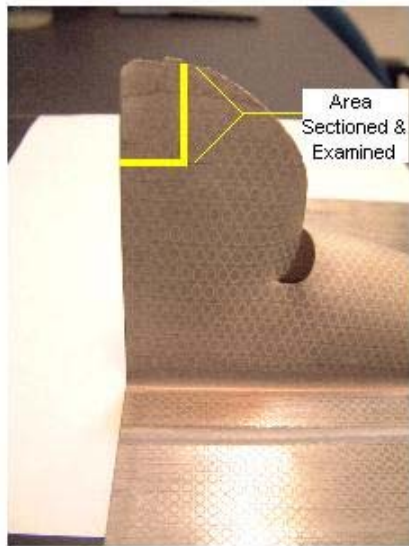
Figure 7. Pictures of fractured PS 978931(K). The picture above reveals where the material under plain strain failed. Bottom pictures shows where the material was sectioned and examined.

D.   SAMPLE PREPARATION

Sample preparation for the various microscopy techniques was conducted using the mechanical polishing scheduled outlined in Table 3. Successively finer silicon carbide abrasives were used during the initial grinding. The silicon carbide papers were place on a rotating wheel and lubricated with a continuous flow of water. Minimal downward force was applied to the sample, and grinding was conducted in one direction until evidence of the prior grinding step was removed. The sample was then flushed with distilled water, rotated 90°, and grinded using the next finer silicon carbide paper. Sample polishing was conducted using rotating wheels with a fastened polishing cloth and using dilute oil-based diamond suspensions. The last mechanical polishing step used a colloidal silica suspension.

Step	Abrasive	Time	RPM
1	500 Grit SiC Paper	30 sec	20
2	1000 Grit SiC Paper	30 sec	20
3	2400 Grit SiC Paper	30 sec	20
4	4000 Grit SiC Paper	30 sec	20
5	3 μm Metadi Diamond Suspension	10 min (2.5 min/axis)	180
6	1 μm Metadi Diamond Suspension	10 min (2.5 min/axis)	180
7	0.05 μm Colloidal Silica	10 min (2.5 min/axis)	90

Table 3. Mechanical Polishing Procedure.

To prevent contamination of the sample's surface, saturation of the polishing wheels with the abrasive solutions was avoided. Using a spray bottle, three squirts of each abrasive solution was applied to the wheel and subsequent drops of distilled water were used during the polishing process for lubrication and dilution. Once again, minimal

downward force was used in polishing to prevent superficial deformation on the sample. After each polishing step, the sample was rinsed with ethanol, placed into a beaker filled with ethanol, and cleaned ultrasonically for ten minutes.

When the mechanical polishing steps were complete, the sample was electropolished to achieve a distortion free surface, which enhances the quality of the electron diffraction pattern. The Buehler Electromet 4 Electro-polisher programmed to 22 volts to achieve a current density of 3.8 A/cm^2 for 10 seconds and an electrolyte solution of 20% $HClO_4$ – 70% C_2H_5OH – 10% Glycerol cooled to 0°C were used. The sample was rinsed in ethanol and either placed directly in the scanning electron microscope (SEM) or stored temporarily in a desiccant container to limit surface oxidation while awaiting examination.

E.   SCHEDULE OF SAMPLE ANALYSIS

The first set of samples evaluated were the ones examined previously in the Maestas' study. According to Figure 8, these samples were sectioned from deformed gauge area 2. The samples were re-polished and, using a permanent ink marker, divided into three regions that were approximately 1.5 cm in length. Areas near the marked regions were then selected for evaluation. The samples were first mounted flat in the scanning electron microscope (SEM), and the Oxford LINK ISIS computer program was used to collect information on the selected area. The samples were then tilted 70° on a mount in the SEM for analysis using the OIM data collection software. The same procedure was implemented to examine deformed gauge areas 1 and 2 from the 978931 uniaxial tension material, as well as, selected regions from the biaxial tension and plane strain material.
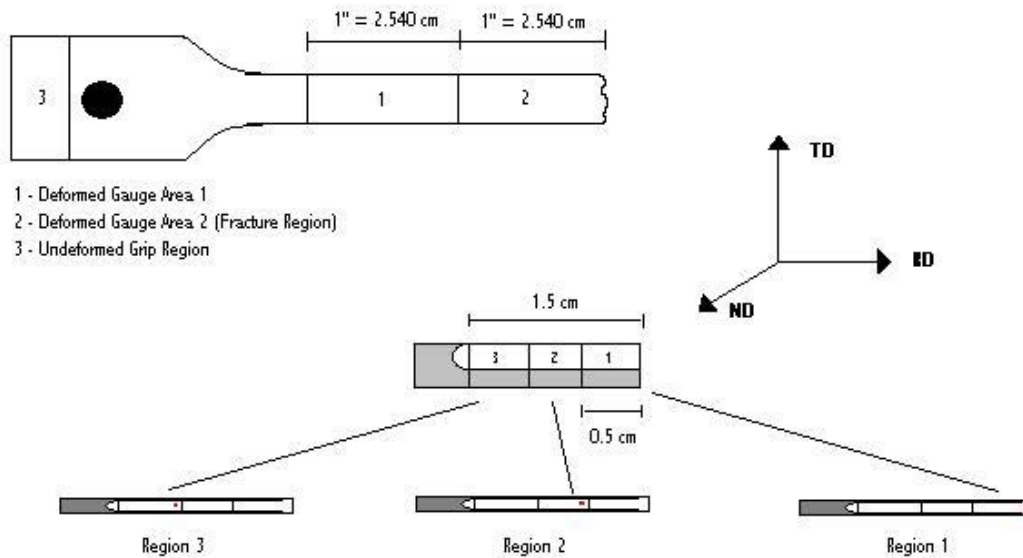
Figure 8. Schematic of areas evaluated for tensile test samples from 978083, 978901 and 978931. The red dots indicate approximate areas where observation took place.

F. ENERGY DISPERSIVE X-RAY ANALYSIS

For the first analysis, a TOPCON SM-510 Scanning Electron Microscope (SEM) equipped with an energy-dispersive x-ray (EDX) detector from EDAX, Inc., and the Oxford Link ISIS software program was used. The system obtained secondary electron (SE) emission images, backscattered electron (BSE) emission images, characteristic energy spectrums, and elemental maps for selected samples. Figure 9 shows a schematic diagram of the origin of electron emissions and X-rays when the specimen interacts with the incident beam.
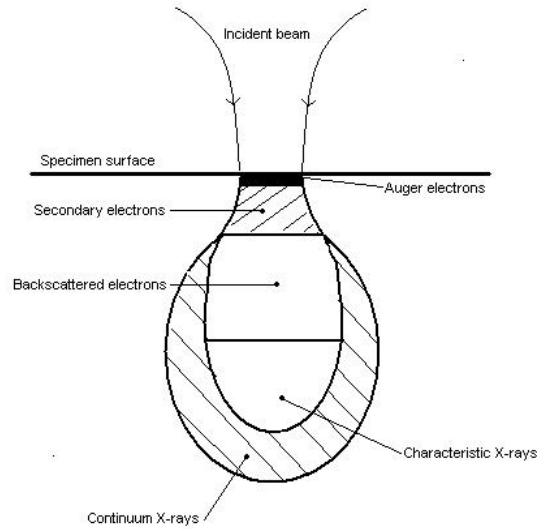
Figure 9. Schematic showing the generation of electrons and X-rays within the specimen. (From: Ref 12)

BSE images were more useful in locating cavities that the SE images. BSE's are electrons that have been back scattered off the surface and thus have higher energies than the secondary electrons (nearer the incident beam energy), as seen in Figure 10. Furthermore, the heavier the atom the higher the energy of the backscatter electrons and the brighter the atom will be on the image. $MnAl_6$ particles were clearly recognized in the BSE images than in the SE images.
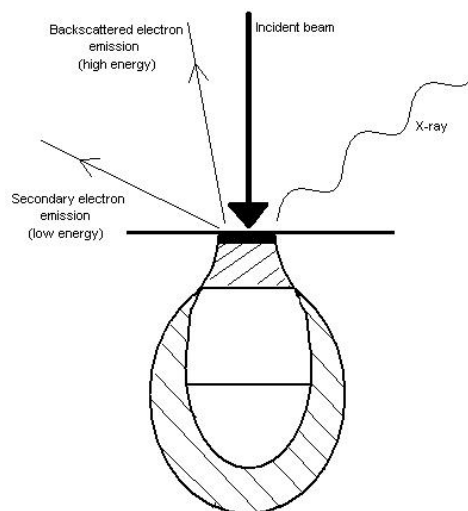
Figure 10. Schematic showing backscattered electrons, secondary electrons and x-rays interaction with the incident beam. (From: Ref 12)

To verify the bright areas were second phase particles, the X-ray Analysis program was used. Elements in the 5083 material were depicted as characteristic energy spectra. Characteristic X-rays are produced when accelerated electrons from the incident beam have sufficient energy to eject one of the inner electrons from its shell. For example when an accelerated electron ejects an electron from the 1s level (K shell), this vacancy is filled by one of the other electrons from an adjacent level (L shell) or higher energy level (M shell). During this transition characteristic X-rays are emitted, K_α X-ray for the former and K_β X-ray for the latter. Figure 11 illustrates this process. Once the elements were identified and labeled, elemental maps were produced using the "speedmap" program. These maps help determine the location of $MnAl_6$ particles and where they were in relation to cavities.   Figure 12 displays an example of a SE image, BSE image and elemental maps for 978931(A3).
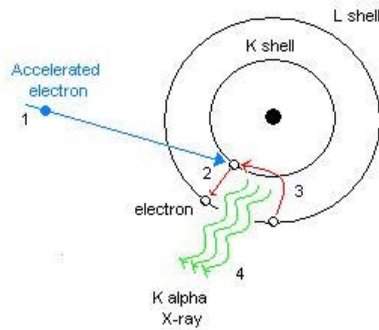
Figure 11. Illustration of how characteristic X-rays is formed. The process is as follows, 1) accelerated electron from incident beam, 2) ejects K-shell electron, 3) L-shell electron fills K-shell electron vacancy, and 4) during transition K_α X-ray emitted.
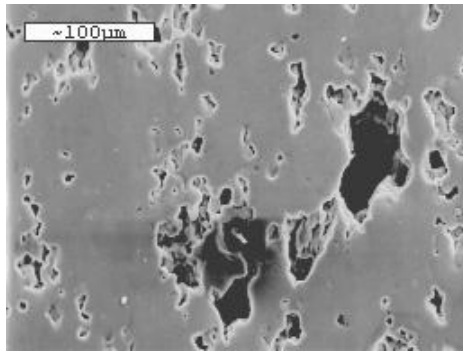
1. SE Image
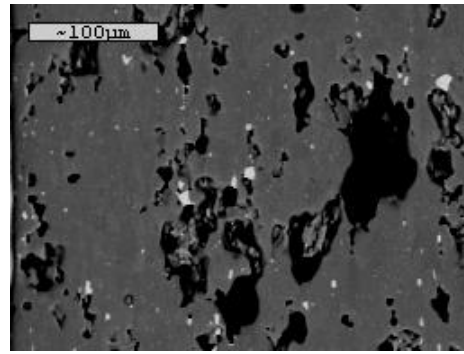
2. BSE Image
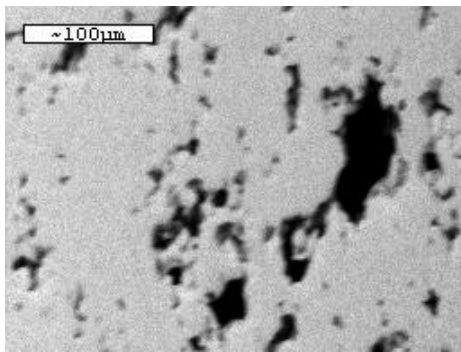
3. Al X-ray (elemental map)
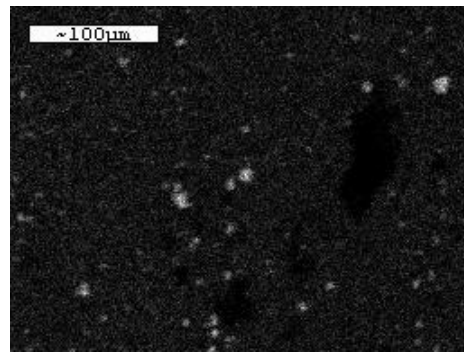
4. Mn X-ray (elemental map)

Figure 12. Images of 978931(A3), deformed gauge area 1- region 1. Sample was pulled under uniaxial tension at 450 °C at a strain rate of $3x10^{-4}$ s^{-1} and elongated to 310% until failure. All images are at 370X. 1. Secondary electron image. 2. Backscattered electron image. Heavier second phase particles appear brighter than lighter aluminum matrix. 3. Aluminum elemental map. 4. Manganese elemental map. The bright areas correlate to the bright areas in the BSE image.

G.   ELECTRON BACKSCATTER DIFFRACTION PATTERN COLLECTION

A TOPCON SM-510 Scanning Electron Microscope (SEM) with a tungsten filament and an accelerating voltage of 20 kV was used to collect electron backscatter diffraction patterns (EBSP). After electro-polishing, the samples were put in the SEM on a mount inclined at 70° to the horizontal, which allows Bragg diffraction conditions to be achieved without rocking the electron beam source. The beam is collimated ("spot mode") and positioned on the area of interest.

When an electron beam of narrowly defined energy strikes the sample at an inclined surface, the electrons disperse beneath its surface, encounter the crystal lattice, and are diffracted in a systematic manner. The diffracted electrons form a pattern composed of intersecting bands that is captured on a phosphor screen in the SEM sample chamber. The bands in the pattern are termed Kikuchi bands and are representative of lattice planes in the diffracting crystal. [Ref. 13]

A low-light charge-coupled device (CCD) camera collects the image of the Kikuchi patterns from the phosphor screen for indexing by the Orientation Imaging Microscopy (OIM) hardware and software from TEXSEM Inc., shown schematically in Figure 13. An image-processing algorithm (Hough Transform) is then used to detect the bands in the diffraction pattern. The pattern can then be indexed by comparing the angles between the detected bands to a table containing known crystal structures. Indexing the pattern allows the crystallographic orientation to be determined for that point. As the beam is moved from point to point, the EBSP will change due to the change in the orientation of the crystal lattice in the diffracting volume [Ref. 14]. The overall outline of the image generation is illustrated in Figure 14.
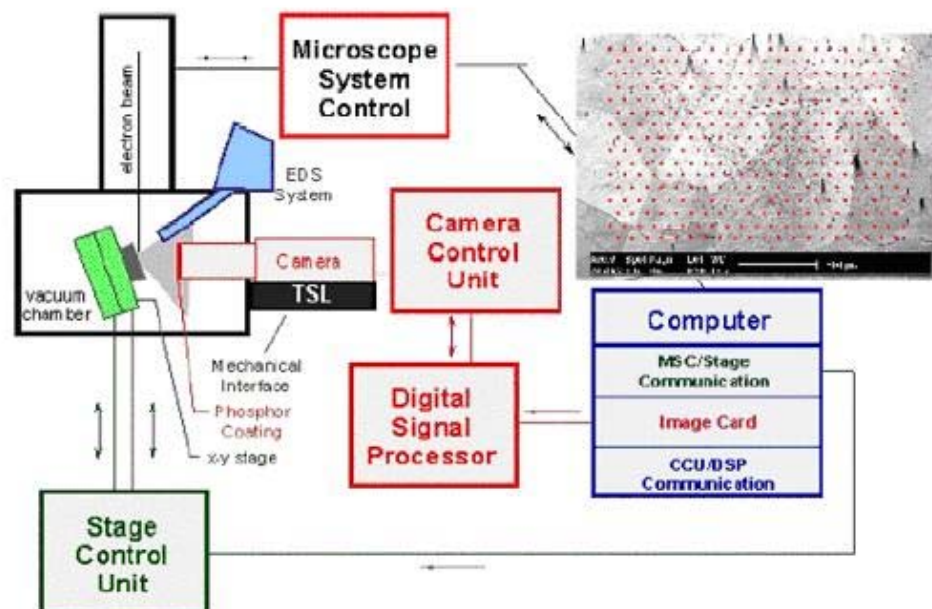
Figure 13. Schematic illustrating the SEM-OIM equipment setup. The top right image illustrates a typical raster pattern used to obtain orientation images. (From: TSL-OIM.com)

27

Data processing in OIM
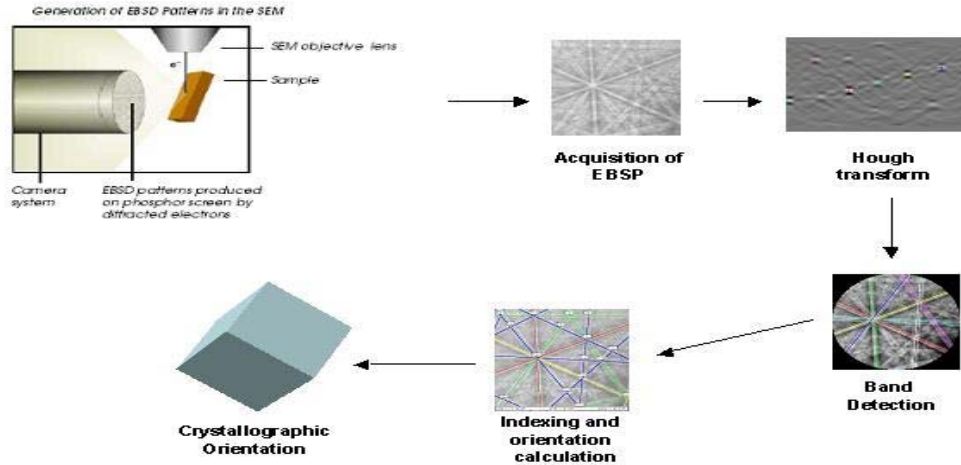
Figure 14. Data processing of the OIM beginning with the raw diffraction pattern, Hough Transform, the resulting detected bands and the final indexed EBSP based on the crystallographic orientation shown. (From: TSL-OIM.com)

The user must instruct the software to calibrate reference patterns to a sample Kikuchi pattern from the material prior to the collection of data. This calibration corrects for distance errors caused by slight mounting variations from one sample to the next that would otherwise cause the line in the reference pattern to be of different length than those generated by the diffraction pattern. For a given diffraction pattern several possible orientations may be found which satisfy the diffraction bands detected by the image analysis routines.

The software ranks these orientations using a voting scheme based on how closely the proposed reference pattern fits the detected Kikuchi bands. The solution that best fits the detected Kikuchi bands is taken as the orientation of the point. The software records the solution in terms of Euler angles in Bunge's form for that pattern. Euler angles (φ_1, Φ, φ_2) in Bunge's form are the three rotations about the principle axes of the crystal that

28

will bring the crystal axes into coincidence with the principle axes of the sample. An illustration of this can be seen in Figure 15. [Ref. 13]
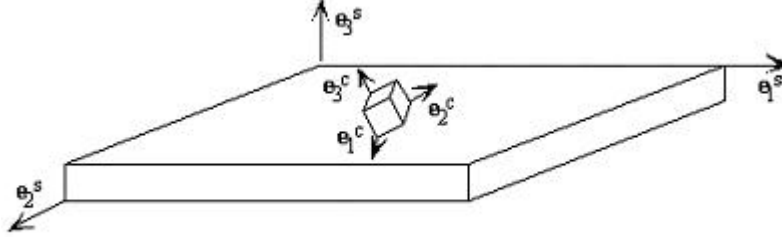
Figure 15. In the case of Bunge's form of the Euler angles (φ_1, Φ, φ_2) this is a rotation (φ_1) about the $\mathbf{e}_3{}^C$ axis followed by a rotation (Φ) about the $\mathbf{e}_i{}^C$ axis followed by a third rotation (φ_2) about the $\mathbf{e}_3{}^C$ axis again. The angles φ_1 and φ_2 range from 0 to 2π and Φ ranges from 0 to π. (From: Ref. 13)

The OIM software also computes two figures of merit for the diffraction data: the confidence index (CI) and the image quality (IQ). The CI is calculated during automated indexing of the diffraction pattern and is based on the voting scheme used in ranking proposed solutions. The software uses the following equation to calculate CI,

$$CI = \frac{(V_1 - V_2)}{V_{Ideal}},$$

where V_1 and V_2 are the number of votes for the first and second solutions and V_{IDEAL} is the total possible number of votes for all possible solutions. The CI ranges from 0 to 1 and CI values greater than 0.1 correspond to a 95% probability that the Kikuchi pattern has been correctly indexed. It should be noted, however, that an EBSP that could not be analyzed is assigned a CI of -1. The CI can be misleading. For example, a confidence index of 0 is obtained when $V_1 = V_2$, yet the pattern may still be correctly indexed. [Ref. 13]

The IQ describes the quality of an electron backscatter diffraction pattern. While the IQ is dependent on the material and it's condition, it is not an absolute value but a function of the technique and parameters used to index the pattern as well as other factors

such as changing conditions in the microscope or video processing (e.g. simply changing the contrast and brightness). The factor affecting the quality of diffraction patterns of most interest, from a materials science standpoint, is the perfection of the crystal lattice in the diffracting volume. Thus, any distortions to the crystal lattice within the diffracting volume will produce lower quality (more diffuse) diffraction patterns. This enables the IQ parameter to be used to give a qualitative description of the strain distribution in a microstructure. However, the IQ parameter has some dependence on orientation. Thus, the IQ cannot be used to distinguish small differences in strain from grain to grain. Nonetheless, the IQ is useful for gaining some insight into the distribution of strain in a microstructure. [Ref. 13]

The electron beam provided by a SEM has a typical diameter range of 50 nm to 150 nm. Therefore, the beam only interacts with a very small volume of the sample relative to typical grain dimensions in engineering material and so the resulting orientation data represents the local lattice orientation at a point within the grain. If the electron beam is displaced from point to point in a pattern on the surface of a sample, the resulting orientation data may be assembled into a map of orientations of the sample surface. The OIM software displaces the electron beam in a hexagonal raster pattern across the sample surface. The size of the scan and step size is user selectable. The software was capable of indexing about 3 points per second, or 10,000 point per hour. The area to be scanned is selected on a secondary electron image of the surface. As the surface of the sample is scanned, data for each point is saved in a single line comprising the Euler angles (φ_1, Φ, φ_2), coordinates relative to the origin of the scanned region (x, y), the IQ, and the CI. The set of data lines corresponding to each point in a scanned region on the sample surface is saved as a *.ang file. This file is the source for all subsequent data analysis. [Ref. 4]

H.   ELECTRON BACKSCATTER DIFFRACTION PATTERN ANALYSIS

One of the unique features of OIM is that the software can assemble orientation data into grain maps. While the concept of a grain in conventional metallography is commonly understood, the definition of a grain in an OIM scan is slightly different. An algorithm groups sets of connected and similarly oriented points into "grains in OIM. For each point in the OIM scan, the neighbors of this point are checked to see if they are oriented within the grain tolerance angle of the given point. In this study, the number of points that define a grain was set at one, while the grain tolerance angle was taken as 2°. If a neighboring point is found to be within the tolerance angle then the neighbors of this point are checked to see if they are within the tolerance angle of this point. The procedure is repeated over and over again until the set of connected grains is bounded by points, which exceed the tolerance angle. Using this approach, the point to point disorientation in a "grain" will be quite small but the spread of orientation among all points in the "grain" can be relatively large. Here disorientation refers to the minimum angle among all crystallographically equivalent rotations necessary to bring adjacent crystal lattices into coincidence. [Ref. 13]

The number of points required to decide whether a given group of points should be considered a "grain" group (the minimum grain size) can be specified by the user along with the grain tolerance angle. Thus, the definition of a grain in OIM can vary depending on user-specified values. An example is shown below in Figure 16, where a grain tolerance angle of 3° was used on the left grain map, while a grain tolerance angle of 15° was used on the right.
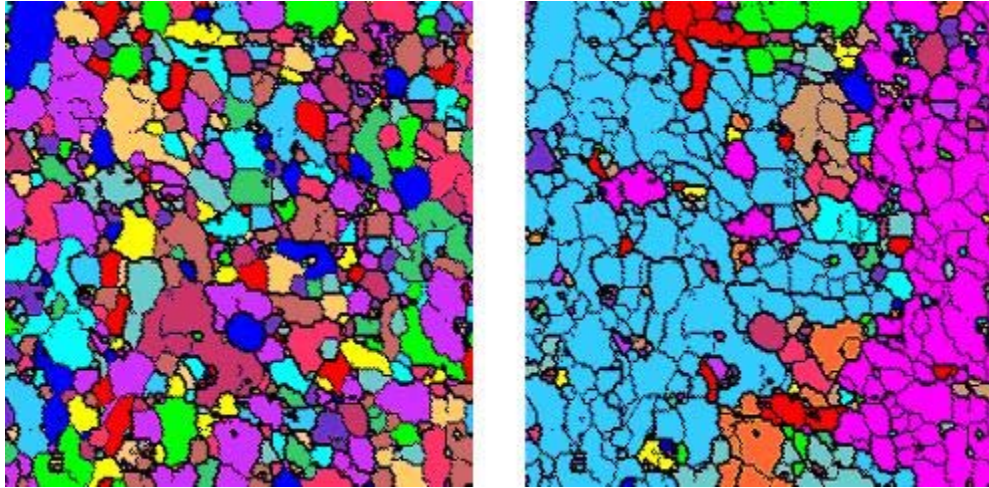
Figure 16. Example of assigning different grain tolerance angles for the same area. The grain map on the left has a grain tolerance angle of 3°, while the right grain map as a grain tolerance angle of 15°. (From: Ref. 13)

As seen in Figure 16, the system assigns a color, at random, to a set of points defined as a grain in accordance with the preceding discussion. It is important to note that the color assigned is not related to the properties of the grain, and, as such, grains that were assigned the same color may or may not have the same orientation associated with them. The importance of each grain being assigned a separate color is to identify the areas in that same colored area that meet the grain tolerance angle criteria from point to point, thereby defining the grains and grain boundaries. Once the grains have been identified, grain-size data may be calculated by determining the area of each pixel and the number of pixels in each grain. For an in depth model of how grain size is calculated see the OIM Analysis User's Manual, page 175-177. [Ref. 13]

Another method to develop a "contrast" mechanism is to generate a grayscale map. In this method, the analysis software assigns a different level of gray proportional to a property that is selected by the operator. For example, an IQ grayscale map will have regions of high IQ depicted by lighter shades of gray and areas that correspond to lower values of IQ will be assigned darker shades of gray. In this manner, areas of high dislocation density, which would have a correspondingly low value of IQ, would appear darker in an IQ grayscale map. An example of an IQ grayscale map is shown in Figure

17. In the figure, an IQ grayscale map is shown next to its color coded counterpart. The OIM software will allow the user to overlay the grayscale map onto the color coded map. [Ref. 13]
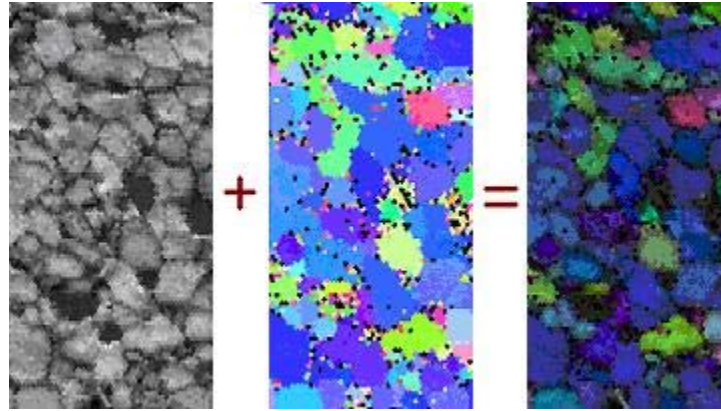
Figure 17. Example of IQ grayscale grain map compared to IQ color coded grain map. The OIM software will allow the user to overlay the maps. (From: Ref. 13)

Additionally, pole figures and disorientation distribution histograms can be directly generated using the orientation data obtained by the collection software. The data obtained in these items can be directly correlated with the grain maps to identify areas of interest by highlighting.

In order to compensate for erroneous data points, cleanup procedures in the OIM analysis software were applied to all scans. Although pattern indexing in OIM is generally quite effective in most regions of a sample surface, the system does have difficulty indexing in some circumstances, e.g. regions of low image quality where Kikuchi bands are diffuse, or nearby grain boundaries where patterns from adjacent grains can superimpose. To deal with such circumstances, three successive cleanup steps were applied to each scan. First, individual points that do not belong to any grains are assigned to match the neighboring majority grain. Second, the highest CI for a grain is assigned to all points in that grain. Third, data points with CI's less than 0.1 are compared to those of nearest neighbors and the neighbor with the highest CI is reassigned to that point, thus effectively making it a point in that grain. This clean-up step assumes

that the low CI points are located near grain boundaries or areas of high dislocation density and that the point with the higher CI is the true orientation for the low CI point.

It should be noted that any single point with a CI greater than 0.1 (95% certainty) will not be altered by this procedure. Grains with good quality EBSP's, no matter what size, will be saved unchanged. The elimination of low CI points was done in order to obtain a true picture of the grain boundaries and the angular disorientation between grains.

IV. RESULTS AND DISCUSSION

A.   OVERVIEW

The results of the study on cavitation in superplastic AA5083 are divided into three parts, according to the stress-state experienced during prior straining. Thus, the first part addresses cavitation under uniaxial tension in the samples designated either 978931(A3) or 978931(A5); the second part analyzes the effect of biaxial stresses in the dome test sample designated 978931(I); and the third part investigates plane-strain conditions in the bulge test sample designated PS 978931(K). Table 4 lists the details of the mechanical testing data for these materials in relation to materials investigated in previous studies.

Material Designation	Temperature Deformation	Strain Rate, $\dot{\varepsilon}$ (s^{-1}) $\dot{\varepsilon}$	Elongation Percentage
978083(A24)	500 °C	3×10^{-4}	205 %
978083(A25)	450 °C	3×10^{-4}	203.5 %
978901(A17)	500 °C	3×10^{-4}	183 %
978901(A20)	450 °C	3×10^{-4}	178.5 %
978931(A3)	**450 °C**	$\mathbf{3 \times 10^{-4}}$	**310 %**
978931(A4)	500 °C	3×10^{-4}	269 %
978931(A5)	**450 °C**	$\mathbf{3 \times 10^{-2}}$	**336 %**
978931(I)	**450 °C**	$\mathbf{1 \times 10^{-2}}$	**Biaxial dome test**
PS 978931(K)	**450 °C**	$\mathbf{1 \times 10^{-2}}$	**Plane-strain bulge test**

Table 4. The mechanical testing data for selected materials investigated for cavitation behavior. Materials examined are in bold text. (Ref.15)

B.   THE STUDY OF CAVITY FORMATION IN A AA5083 MATERIAL UNDER UNIAXIAL TENSION

Two uniaxial tension samples, designated 978931(A3) and 978931(A5), were selected for this investigation. From Table 4, these materials had been deformed at the same temperature, but at different strain rates. Accordingly, the diffusion coefficient, D_L,

35

in equation 2.5 is constant. As seen in Figure 18, the 978931(A3) material had been deformed in the GBS regime $(n \cong 2$ or $m \cong 0.5;$ see equation 2.5$)$, whereas the 978931(A5) material had been deformed in the dislocation deformation regime $(n \cong 4$ or $m \cong 0.25;$ see equation 2.5$)$. Preliminary OIM analysis suggests that this is the case. In Figure 19(b), pole figures for 978931(A3) reveal a random microtexture, and the disorientation histogram containing a large amount of high angle boundaries. This finding is consistent with microtextures found in materials deformed in the GBS regime. [Ref. 15, 17] In Figure 19(a), pole figures for 978931(A5) reveal <100> and <111> components in a fiber texture, and the disorientation histogram contains a noticeably higher amount of small angle boundaries. This finding is consistent with microtextures found in materials deformed in the dislocation deformation regime. [Ref. 15, 17]

A more detailed examination was performed on two areas in the deformed gauge region of the 978931(A3) material and on one area in the deformed gauge region of the 978931(A5) material. In the first material, an area away from the fracture point was chosen to study the initial stages of cavity formation. Referring to Figure 5, this region was designated 978931(A3)-deformed gauge area 1, region 2 (A3-1-2). The second area, located near the fracture point, was selected to study the final stages of cavity formation, and was designated 978931(A3)-deformed gauge area 2, region 2 (A3-2-2).   In the second material, an area also located near the fracture was chosen to be analyzed, and was designated 978931(A5)-deformed gauge area 2, region 2 (A5-2-2).

An OIM analysis of the A3-2-2 region was first conducted to assess the material's microstructure and microtexture. The IQ grayscale map in Figure 20(a) exhibits a microstructure that consists of fine, equiaxed grains. There are also large cavities, reflecting that the region is indeed near the fracture point, as well as some smaller cavities. The microtexture data in Figure 20(b) reveals a near-random texture in all of the pole figures. Prior investigations have shown that a B-type texture ({110}<112>, where {rolling plane} and <rolling direction>) develops during cold rolling prior to recrystallization annealing.
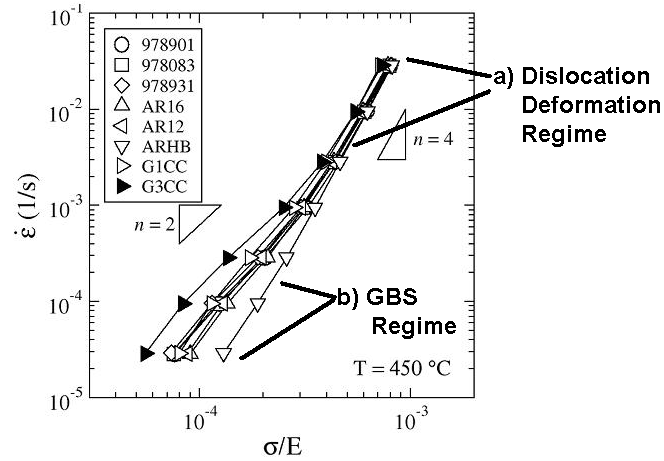
Figure 18. Modulus-compensated stress versus strain rate data characterizing mechanical behavior for various AA5083 materials. a) Dislocation Deformation Regime. b) GBS Regime. The three materials of interest are 989901, 978083 and 978931.   All three behave similarly in the mechanical sense. Data and plot from University of Texas-Austin, TX. (From: Ref. 15)
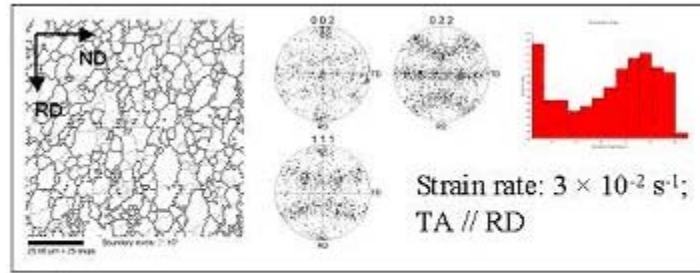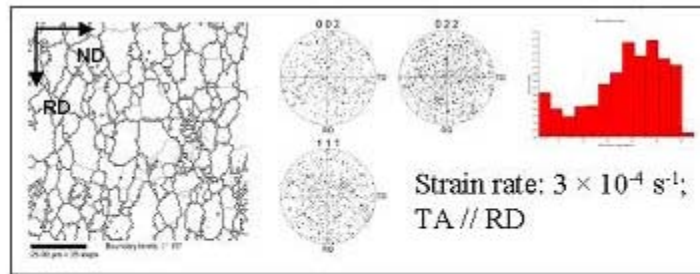
Figure 19. a) 978931(A5). Distinct fiber texture in <100> and <111>, and large amounts of small angle grain boundaries verifies that the material was deformed in the dislocation deformation regime. b) 978931(A3). Random microtexture verifies that the material was deformed in the GBS regime.

37

Upon heating and annealing prior to elevated temperature deformation particle-stimulated nucleation of recrystallization results in the formation of a predominately random texture. Retention of this random texture (Figure 20(b)) indicates that the dominant deformation mechanism is GBS. [Ref. 17] In Figure 20(c), grain boundaries of disorientation > 15° surround equiaxed grains. The disorientation histogram in Figure 20(d) verifies that the microstructure consists mainly of high-angle boundaries associated with essentially random grain lattice orientations. Other materials, such as 978083 and 978901, exhibit essentially identical microstructures and microtextures when deformed in uniaxial tension at 450°C at 3×10^{-4} s^{-1}. [Ref. 5] Thus, all three variants of AA5083 have responded in the same manner to processing and elevated temperature deformation, as well as performing similarly in a mechanical sense, as seen in Figure 18.

The OIM analysis conducted on A5-2-2 produced distinctly different results. As seen in Figure 21, the grains appear smaller and with a lower IQ overall indicative of higher strain energy.[Ref. 4] The microtexture is revealed using discreet poles figures, Figure 21(b). A definite two-component deformation texture is present, with a distinct <111> fiber evident on the {111} pole figure and a <100> fiber texture component forming as shown in the {002} pole figure. The distribution of orientations at 90° to RD, which is the tensile axis in the {002} pole figure, suggests a weak {001}<100> component as well. This type of microtexture is consistent with the microtexture found in AA5083 that were subjected to dislocation creep controlled strain conditions. [Ref. 4, 5,17] The high population of small-angle (0°-5°) boundaries seen in Figure 21(d) validates that the material was deformed in the dislocation deformation regime.

SE images, BSE images and elemental maps were obtained for each area to locate cavities and identify MnAl$_6$ particles. In Figure 22, the SE and BSE images, as well as the Al and Mg X-ray maps of the A3-1-2 sample show numerous small, equiaxed cavities. The bright particles evident in the Mn X-ray map correspond to the dispersed MnAl$_6$ particles distributed throughout the BSE image. Careful examination of the BSE

image shows that many of the cavities are associated with $MnAl_6$ second phase particles, suggesting that the cavities were indeed formed in association with these particles. However, a few cavities are not apparently associated with second phase particles, indicating either that cavity formation may occur in the absence of particles or that the particles are not resolved by BSE imaging.

Similar results were observed in the A3-2-2 region. In Figure 23, the larger cavities reflect the progressive growth and linkage of smaller cavities during straining in this region near the final fracture. The images again show that some of the cavities are clearly associated with $MnAl_6$ particles while others are formed, likely by grain boundary separation, possibly in the absence of particles. In particular, the largest cavity does not appear to have any $MnAl_6$ particles present. Although the BSE image indicates the presence of particles within the cavity, those particles do not correlate with Mn X-ray map. In this instance the bright features in the large cavity were found to correlate with silicon-containing particles likely entrapped from the colloidal silica suspension used in the mechanical polishing process. Ultrasonic rinsing and electro-polishing apparently failed to clean the cavity. The also raises the possibility that second phase particles may have been pulled out during the mechanical polishing process.
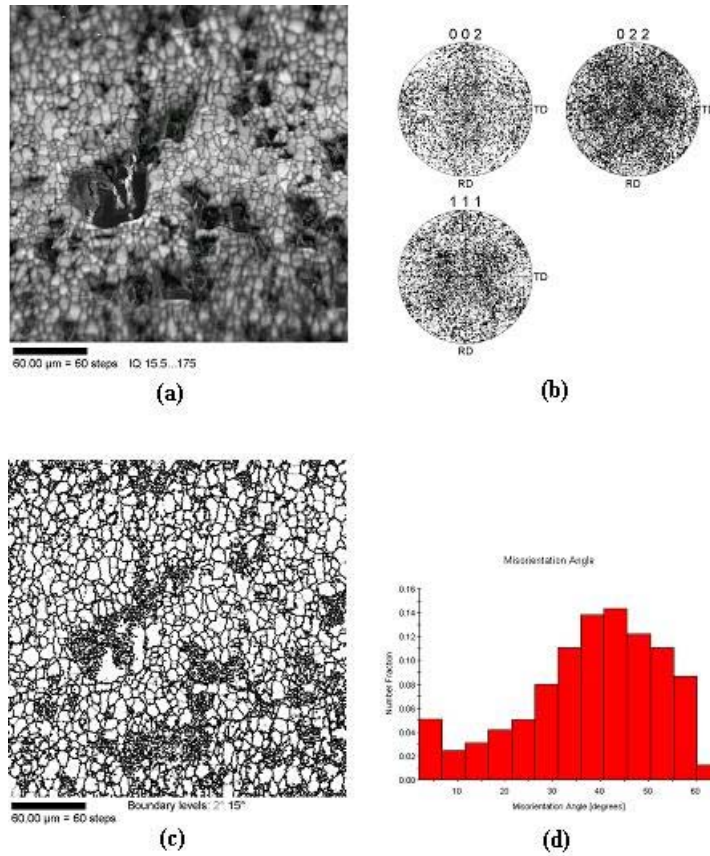
Figure 20. Microstructure and microtexture data for 978931(A3), deformed gauge area 2, region 2 (A3-2-2). (a) Relatively fine equiaxed microstructure is evident in the IQ grayscale map. (b) Pole figures reveal a randomly distributed microtexture. (c) Grain boundary map indicates a dominance of high angle boundaries (>15º) throughout the microstructure. (d) The grain-to-grain disorientation distribution confirms both the pole figure and grain boundary map data.

Figure 21. Microstructure and microtexture data for 978931(A5), deformed gauge area 2, region 2 (A5-2-2). (a) Fine equiaxed microstructure is evident in the IQ grayscale map. (b) Pole figures reveal distinct <111> and <100> fiber textures. (c) Grain boundary map indicates a dominance of high angle boundaries (>15°) throughout the microstructure. (d) The grain-to-grain disorientation distribution confirms both the pole figure and grain boundary map data, and the large population of low-angle boundaries (0°-5°) is consistent with subgrain formation during dislocation creep.

Figure 22. Secondary electron image, backscatter electron image and X-ray maps for Al, Mg and Mn for 978931(A3), deformed gauge area 1, region 2 (A3-1-2). Higher volume fraction compared to dislocation deformation. Cavities are more nearly equiaxed. Many cavities are not obviously associated with particles.

Figure 23. Secondary electron image, backscatter electron image and X-ray maps for Al, Mg and Mn for 978931(A3), deformed gauge area 2, region 2 (A3-2-2). Larger cavities are located throughout the region. Many cavities are not obviously associated with particles.

Although the 978931(A5) material was deformed under dislocation deformation conditions, observations regarding particle association with cavities were the same as for the 978931(A3) material. Region A5-2-2, as shown in Figure 24, has a small cavity volume fraction when compared to the material that had been deformed in the GBS regime. In the BSE image, some cavities seem to form in association with particle stringers, while many others are not obviously associated with particles. It is apparent from all three EDX analysis that the $MnAl_6$ second phase particles serve as nucleating sites for cavities, as also cited by Taleff. [Ref. 9] However, some cavities are not obviously associated with cavities; this may reflect separation of boundaries in the absence of particles, or insufficient resolution of the particles in the BSE images.
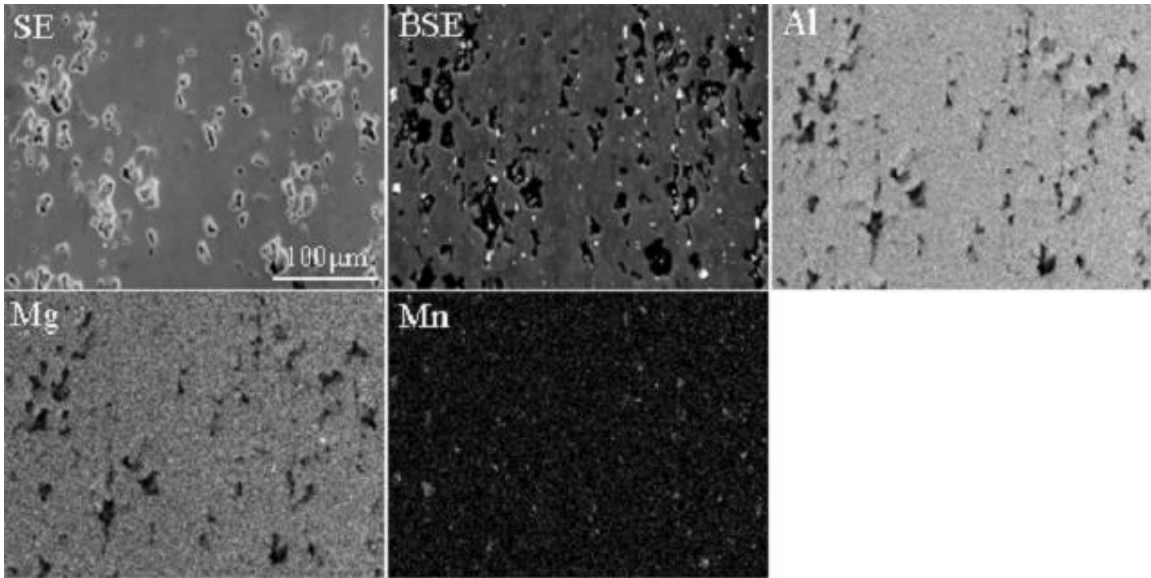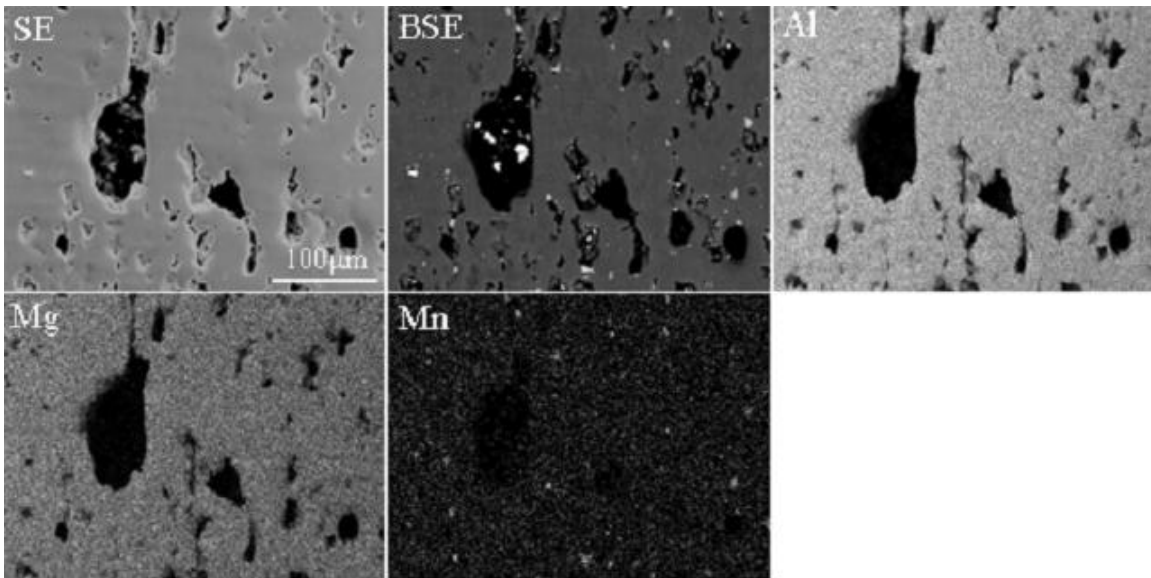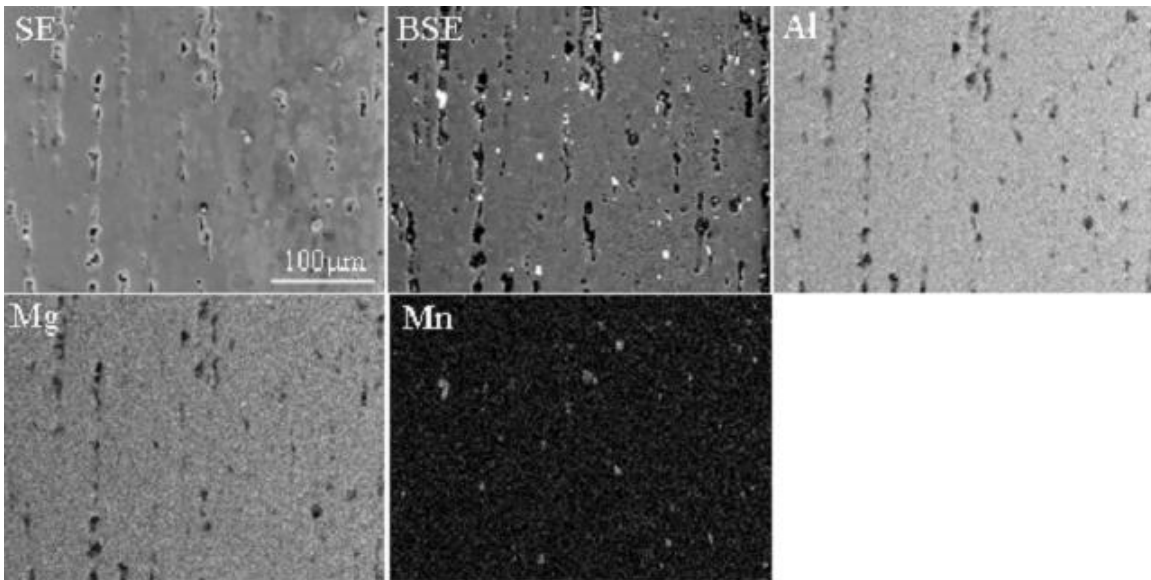

Figure 24. Secondary electron image, backscatter electron image and X-ray maps for Al, Mg and Mn for 978931(A5), deformed gauge area 2, region 2 (A5-2-2). Small volume fraction compared to GBS regime. Cavities are formed in association with stringer particles. Many cavities are not obviously associated with particles.

Subsequently, and following Maestas' research, the nature of the boundaries that apparently had failed, thereby resulting in cavity formation, was examined. It is assumed that small cavities are newly formed, and that grain-to-grain orientation relationships reflect boundary disorientations of sliding boundaries prior to separation of the boundaries as the cavities form. Using a method similar to Maestas', the grain-to-grain disorientation distributions across cavities in 978931(A3) were evaluated. The 978931(A5) was not evaluated in this regard due to the small number of fine cavities in it. Figure 25 shows the scanned areas using both EDS and OIM. A region 275μm × 275 μm in size was selected to cover most of the area imaged in EDS in order to enable direct comparison of these characterization methods and to verify that areas of low image quality in OIM images match the cavities resolved in the EDS images. As illustrated in Figure 26, 100 μm × 100 μm areas within the larger region were subsequently scanned to evaluate cavities of size ≤ the size of surrounding grains. Throughout the material, grains surrounding such small cavities were selected using the "grain mode" highlighting feature in the OIM analysis software. The lattice orientations and grain-to-grain disorientations across the cavity were recorded using "point mode" highlighting, and results were plotted on a histogram shown in Figure 27.

The histogram reveals similar results distributions similar to those reported by Maestas. The distributions are similar to those of annealed and recrystallized material except that there are no disorientations < 7°. Such a value is consistent with a threshold value of disorientation for GBS in pure aluminum as reported by Weinberg [Ref. 15]. However these results do not expose the role of second phase particles in cavity formation.
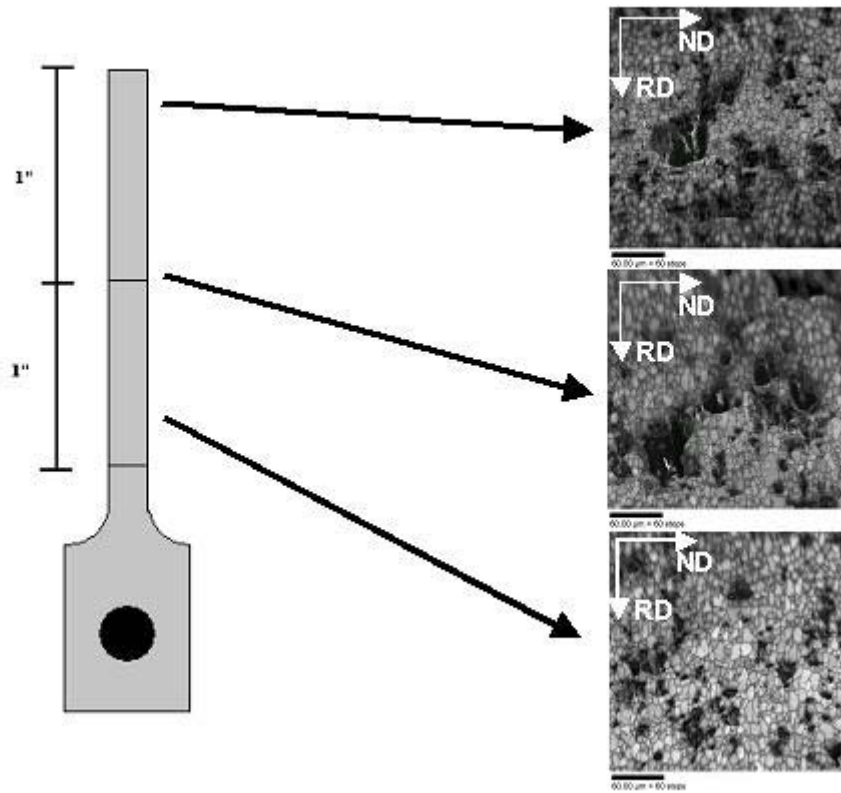
Figure 25. An illustration of "step down" method used on sample 978931(A3). The top micrograph is of area A3-2-2; the middle is of area A3-1-1; and the bottom is of A3-1-2.
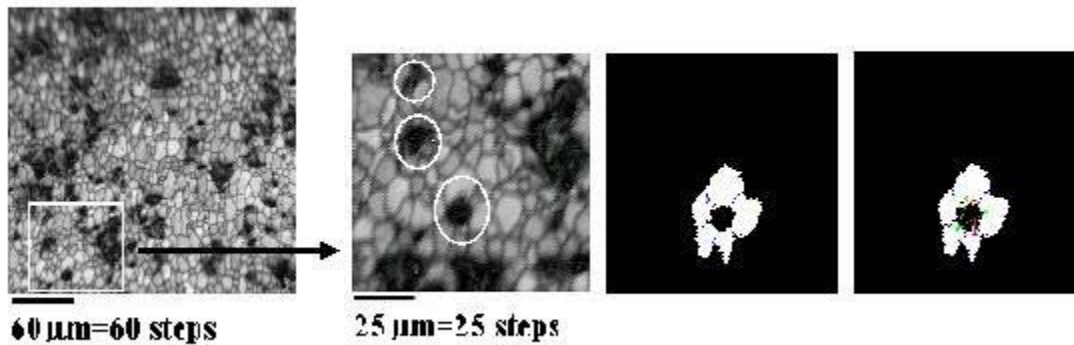
Figure 26. Determination of grain orientation relationships for small cavities for 978931(A3) material. A 100 μm^2 section within the 275 μm^2 region for A3-1-2 was scanned, and surrounding grains around small cavities were highlighted. The lattice orientations, disorientations across the cavity were evaluated and plotted on a histogram.
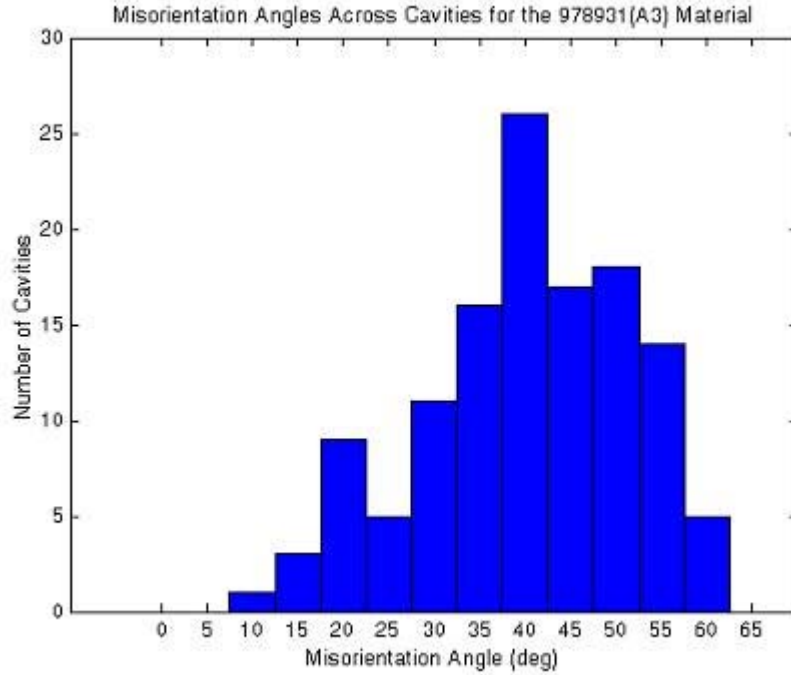
Figure 27. Histogram showing the distribution of cavities as a function of disorientation angle for the 978931(A3) material deformed at 450 ºC at 3×10^{-4} s^{-1}.

C. THE STUDY OF CAVITY FORMATION IN A AA5083 MATERIAL UNDER BIAXIAL TENSION

Two areas of the biaxial dome sample, designated 978931(I), were also examined in this study of cavitation behavior. As shown in Figure 28, the first area examined, designated here as I-1, is located approximately 15° from the pole of the dome, and the second area, designated I-3, is located essentially at the pole. As for samples from material tested in uniaxial tension, BSE micrographs and EDS data were first assessed for association of second phase particles and cavitation, and then the disorientation distributions across cavities were evaluated. The data also enable the evaluation of texture development during biaxial straining.

An OIM analysis was performed on the two areas in order to determine the microstructure and microtexture of the material. In Figures 29 & 30, the results of this

analysis are essentially the same for both I-1 and I-3. The microstructure revealed in the IQ grayscale map of both regions consists of equiaxed grains, as seen in Figures 29(a) & 30(a). However, the cavities tend to be larger and more nearly equiaxed in shape than the cavities found under uniaxial straining conditions at corresponding strain rates in the dislocation deformation regime. Microtexture data in the form of pole figures, as shown in Figures 29(c) & 30(c), show a distinct deformation texture. There is a strong <001> fiber, and a weak <110> fiber (in this notation, <uvw> is the crystal direction parallel to the local outward normal of the dome). The development of a deformation texture here under biaxial straining conditions is consistent with the development of a deformation texture during uniaxial deformation under dislocation creep controlled strain. Under biaxial conditions, however, the axis of symmetry in the texture (the fiber axis) aligns with the local dome normal. In contrast, the fiber axis under uniaxial tension aligns with the tensile axis. The disorientation distribution plots found Figure 29(d) & 30(d) suggest the superposition of a low angle (0º - 5º) peak, reflecting dislocation accumulation and subgrain formation, and a Mackenzie-random distribution dominated by high angle boundaries. [Ref. 18]

These same areas were analyzed using BSE imaging and EDS. The X-ray maps, again, were obtained to examine the role of the $MnAl_6$ second phase particles in cavity formation and growth. Figure 31 shows the SE and BSE images and elemental maps for I-1. As noted in the IQ grayscale map, there are larger and more nearly equiaxed cavities when compared to uniaxial tension sample deformed under dislocation deformation conditions. While many cavities clearly form in association with stringers of particles, some cavities are apparently not associated with particles. From Figure 32, similar results and conclusions can be drawn from the EDS images for I-3.
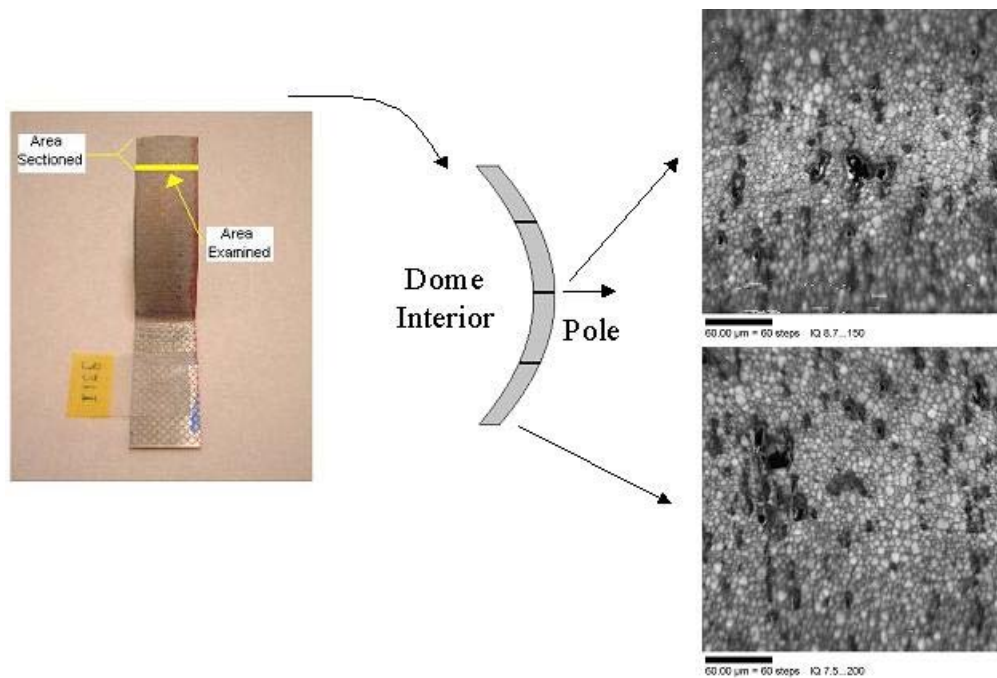
Figure 28. Display of areas scanned in the biaxial dome test sample 978931(I) deformed at 450°C at $1x10^{-2}$ s^{-1}. The top IQ grayscale map is an area near the pole, designated I-3, and the bottom grayscale map is an area approximately 15° from the pole, designate I-1.
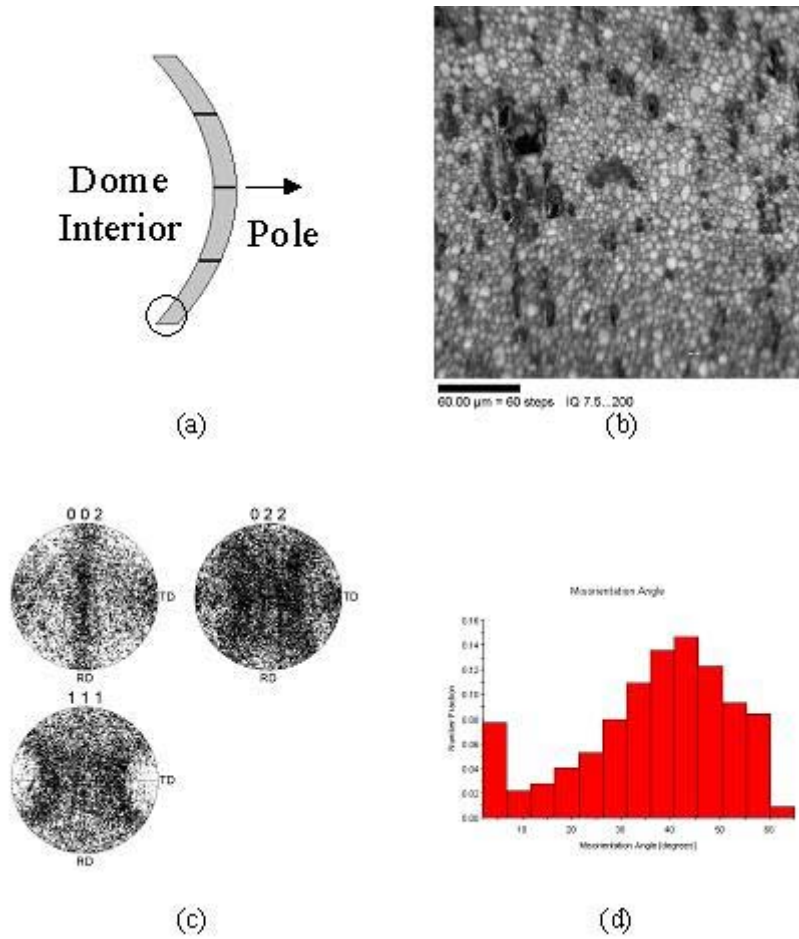
Figure 29. Microstructure and microtexture data for the 978931(I) ~15° from the pole: biaxial dome test at 450°C, 1×10^{-2} s^{-1}. (a) Location of the approximate location of the OIM scan. (b) IQ grayscale map exhibits relatively fine equiaxed microstructure. (c) Pole figures revealing strong fibers in <001> and weak fibers in <110> (<uvw> is direction parallel to outward normal). (d) Histogram of disorientation angles reveals the high degree of high angle boundaries associated with the microstructure.
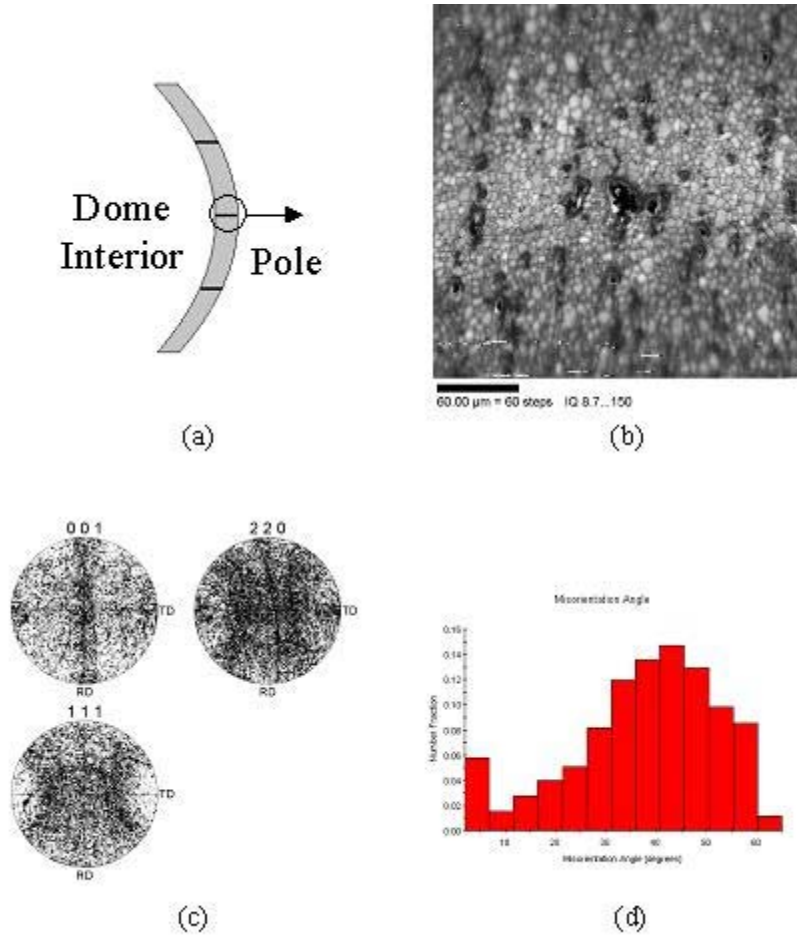
Figure 30. Microstructure and microtexture data for the 978931(I) near the pole: biaxial dome test at 450°C, $1x10^{-2}$ s^{-1}. (a) Location of the approximate location of the OIM scan. (b) IQ grayscale map exhibits relatively fine equiaxed microstructure. (c) Pole figures revealing strong fibers in <001> and weak fibers in <110> (<uvw> is direction parallel to outward normal). (d) Histogram of disorientation angles reveals the high degree of high angle boundaries associated with the microstructure.

Figure 31. SE, BSE and Al, Mg and Mn X-ray maps of biaxial dome test sample 978931(I) ~15° from the pole; deformed at 450°C, $1x10^{-2}$ s^{-1}– dislocation deformation by solute drag creep.
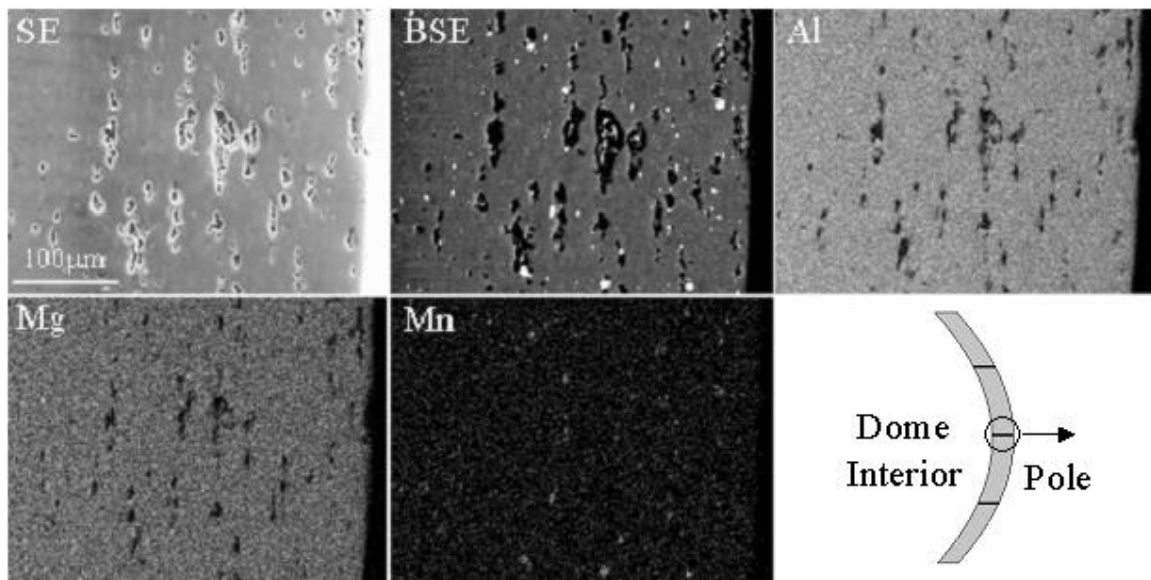
Figure 32. SE, BSE and Al, Mg and Mn X-ray maps of biaxial dome test sample 978931(I) near the pole; deformed at 450°C, $1x10^{-2}$ s^{-1}– dislocation deformation by solute drag creep.

Using the method outlined in the previous section, grains surrounding small cavities were highlighted and the lattice disorientations across the cavities were evaluated. Figure 33 illustrates this process and shows a histogram of approximately 150 disorientations across such cavities. As found for small cavities in material deformed in uniaxial tension, the disorientation distribution across cavities is similar to the Mackenzie random distribution except that there are no boundaries of disorientation < 7º. This threshold for cavity formation is consistent with the occurrence of GBS prior to boundary separation and, furthermore, suggests that GBS contributes to cavity formation even when deformation is controlled by dislocation deformation mechanisms – e.g. solute drag creep.
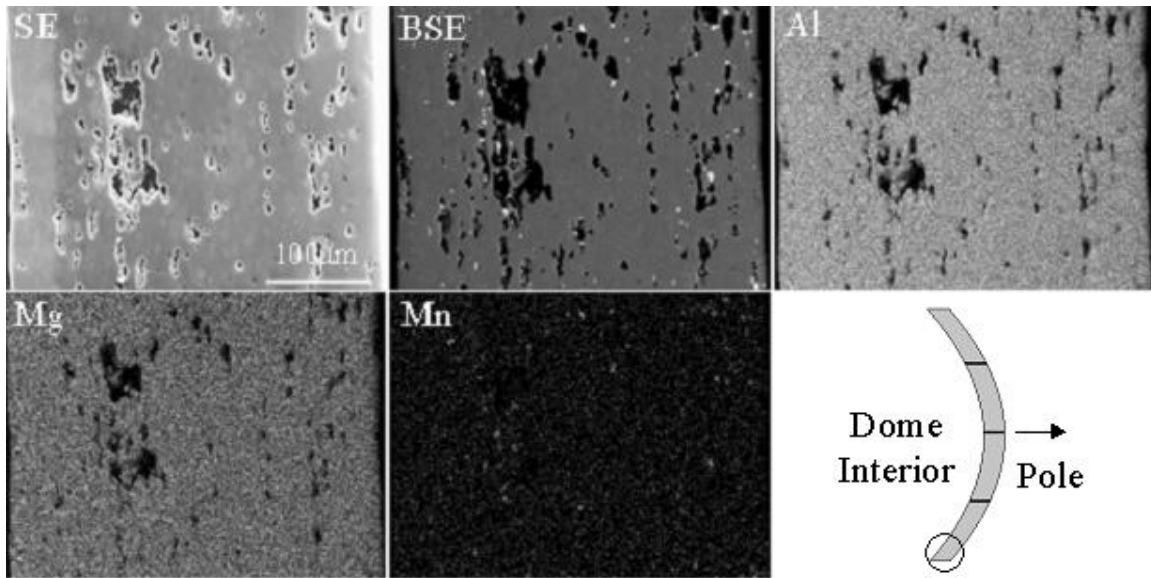

Figure 33.   978931(I)~15° from the pole: Biaxial dome test at 450°C, 1×10^{-2} s^{-1}. Histogram showing the distribution across small cavities as a function of disorientation angle for the biaxial dome test material 978931(I).

D. THE STUDY OF CAVITY FORMATION IN A AA5083 MATERIAL UNDER PLANE STRAIN

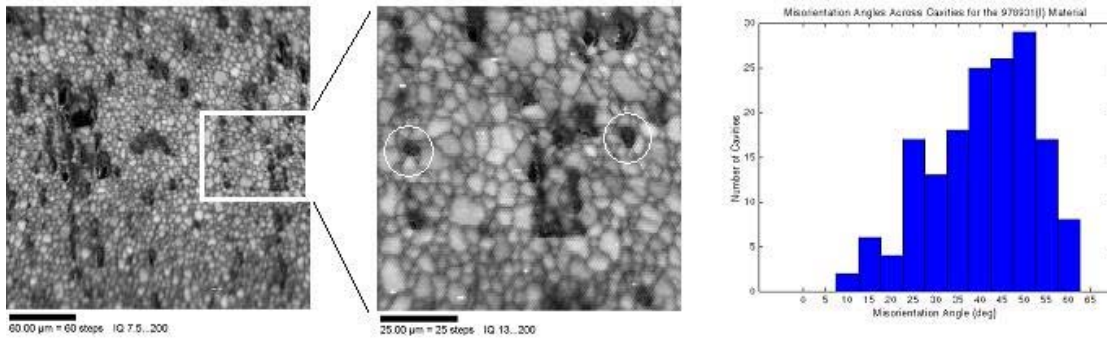Two areas of the plane strain bulge material 978931(K) were examined for the final part of this study of cavitation behavior. As shown in Figure 34, the first area evaluated, designated K-1, is located near the fractured region, and the second area, designated K-2, is located near the middle of the sample. As with the other two studies, microstructure and microtexture examination, the role of second phase particles in cavitation, and the nature of grain boundaries were analyzed.
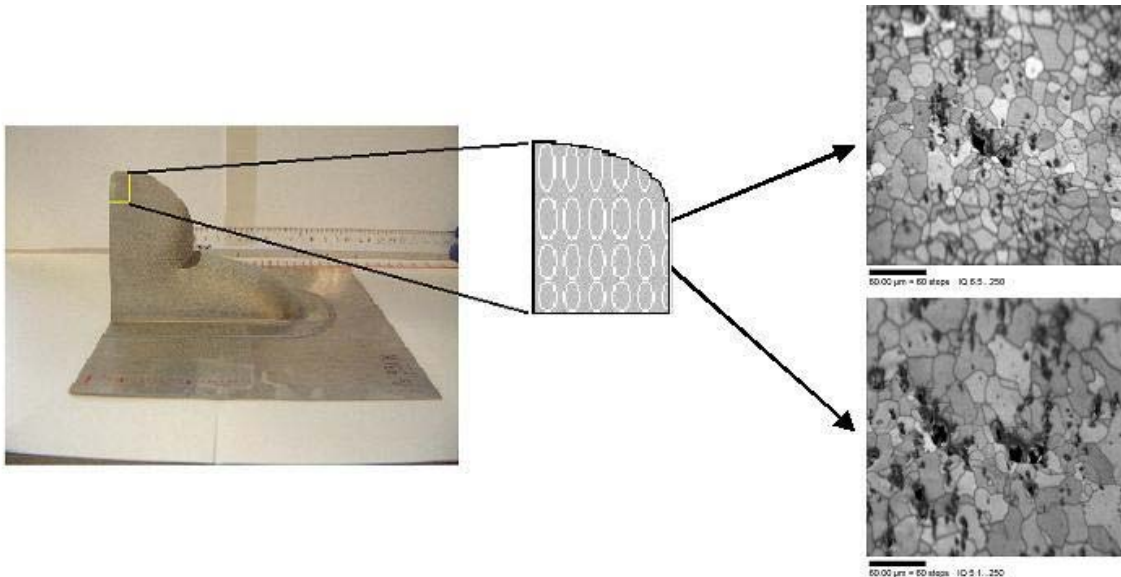
Figure 34. Display of areas scanned in the biaxial dome material 978931(K) deformed at 450 °C, 1 x 10^{-2} s^{-1}. The top IQ grayscale map is located near the fracture and is designated K-1. The bottom IQ grayscale map is located near the center of the material and is designated as K-2. The grain size in 978931(K) is considerably coarser than in 978931(I).

These locations in the plane strain sample experienced differing local strains (and strain rates) although having been deformed under a nominal rate of $1x10^{-2}$ s^{-1}. This is evident in the different sizes of the ellipses on the surface of the material. Before

deformation, a pattern of circles, 2.50 mm in diameter, was applied by a photoresist method on the sheet surface of the AA5083 aluminum. As subsequent deformation took place due to differential pressure, the circles evolved into ellipses as the sheet deformed. Figure 35 shows that larger ellipses indicate high local strain rates, as in the case of K-1, and smaller ellipses indicate low local strain rates, as in the case of K-2.
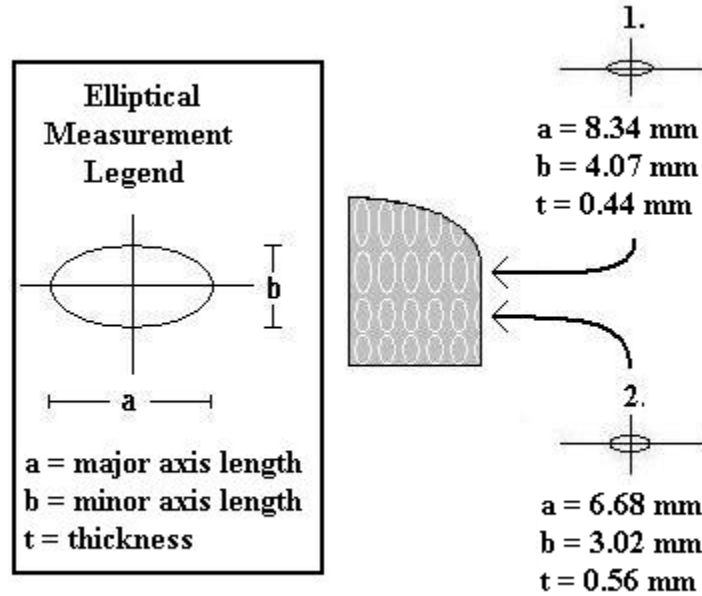
Figure 35. Elliptical measurements from plane strain dome material 978931(K) deformed at 450 °C at 1 x 10^{-2} s^{-1}. 1. Ellipse located in the vicinity of K-1. High local strain accounts for the enlargement of the ellipse in this area. 2. Ellipse located in the vicinity of K-2. Low local strain account for the smaller size of the ellipse in this area.

The OIM analysis conducted on these two areas illustrates effects associated with these strain differences. Comparing the IQ grayscale image in Figure 36(a) to that in Figure 37(a), the K-1 location exhibits smaller equiaxed grains than at K-2. However, the grain size in either case is much coarser than in the 978931(I) material, although the grains are equiaxed. This microstructure is similar to that observed in uniaxial tension material, A3-2-2, deformed under 450°C at 3x10^{-4} s^{-1} in the GBS regime. The pole figures in Figure 36(b) all exhibit a predominantly random texture although a weak

54

<100> fiber can also be seen. The disorientation histogram in Figure 36(c) shows a predominance of high angle boundaries. Altogether, these results all suggest that GBS has had a major role at this stage of deformation in the K-1 area despite the nominal straining conditions that correspond to the dislocation deformation regime. [Ref. 17]

Rather different results were obtained in the OIM analysis of the K-2 region. As mentioned previously, the IQ grayscale image in Figure 37(a) shows a microstructure that consists of larger grains. The pole figures in Figure 37(b) exhibit a predominate random component but careful examination reveals the development of a <100> fiber orientation as well. As with K-1, the disorientation histogram in Figure 37(c) indicates mainly high angle boundaries; however, there are now a relatively large number of low angle boundaries as well, consistent with a significant contribution of dislocation deformation in this region while GBS has had a lesser role. [Ref. 17]

Despite these differences in the relative contributions of these deformation mechanisms the cavitation study found that cavity development and growth in the two areas mirror each other. The role of $MnAl_6$ second phase particles in cavity formation was once again investigated by analyzing the EDS images. Figure 38 and 39 show the SE, BSE and elemental maps for K-1 and K-2, respectively. As with the preceding cavitation studies, the cavities often form in association with either isolated particles or with particle stringers. Again, some cavities are apparently not associated with particles. Using the method outlined in the uniaxial tension section, grains surrounding small cavities were highlighted and the lattice disorientations across the cavities were evaluated. Figure 40 illustrates this analysis and shows a histogram of approximately 150 disorientations across cavities. The disorientation distribution across cavities is consistent with GBS (there is a ~7° threshold for cavity formation). This suggests that GBS contributes to cavity formation even when deformation is controlled by dislocation deformation mechanisms, e.g. solute drag creep.
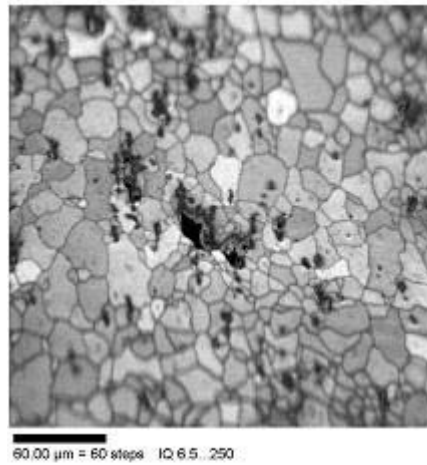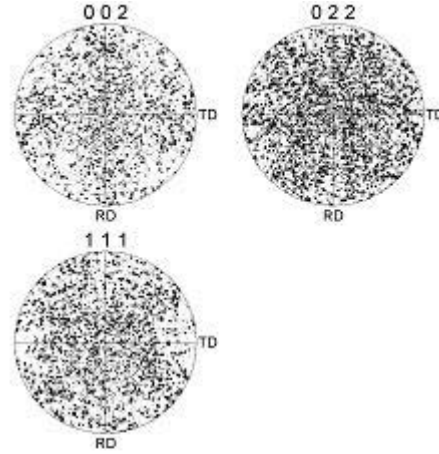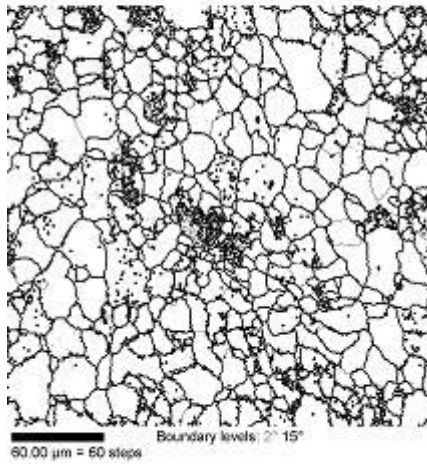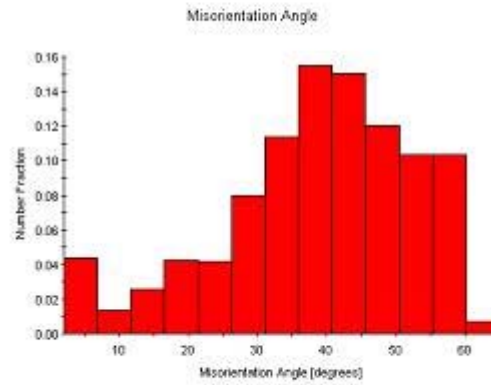
Figure 36. Microstructure and microtexture data for the 978931(K)-1, 450 °C, 1 x 10^{-2} s^{-1}. (a) Location of the approximate location of the OIM scan. (b) IQ grayscale map exhibits relatively fine equiaxed microstructure. (c) Pole figures revealing a random microtexture with weak <100> fibers. (d) Histogram of disorientation angles reveals the high degree of high angle boundaries associated with the microstructure.

Altogether, these results suggest that GBS is the principal mechanism leading to cavity formation on boundaries. Cavities may form due to inadequate accommodation of particles as sliding occurs on particle-containing boundaries, and cavities may also form when GBS in inadequately accommodated at grain boundary triple junctions in the absence of particles on a particular boundary. Furthermore, GBS is apparently the mechanism of cavity formation even during deformation under dislocation creep controlled conditions. Biaxial and plane strain conditions result in increased cavity formation in comparison to uniaxial conditions, most likely because of increased triaxiality leading to an increased contribution of GBS.
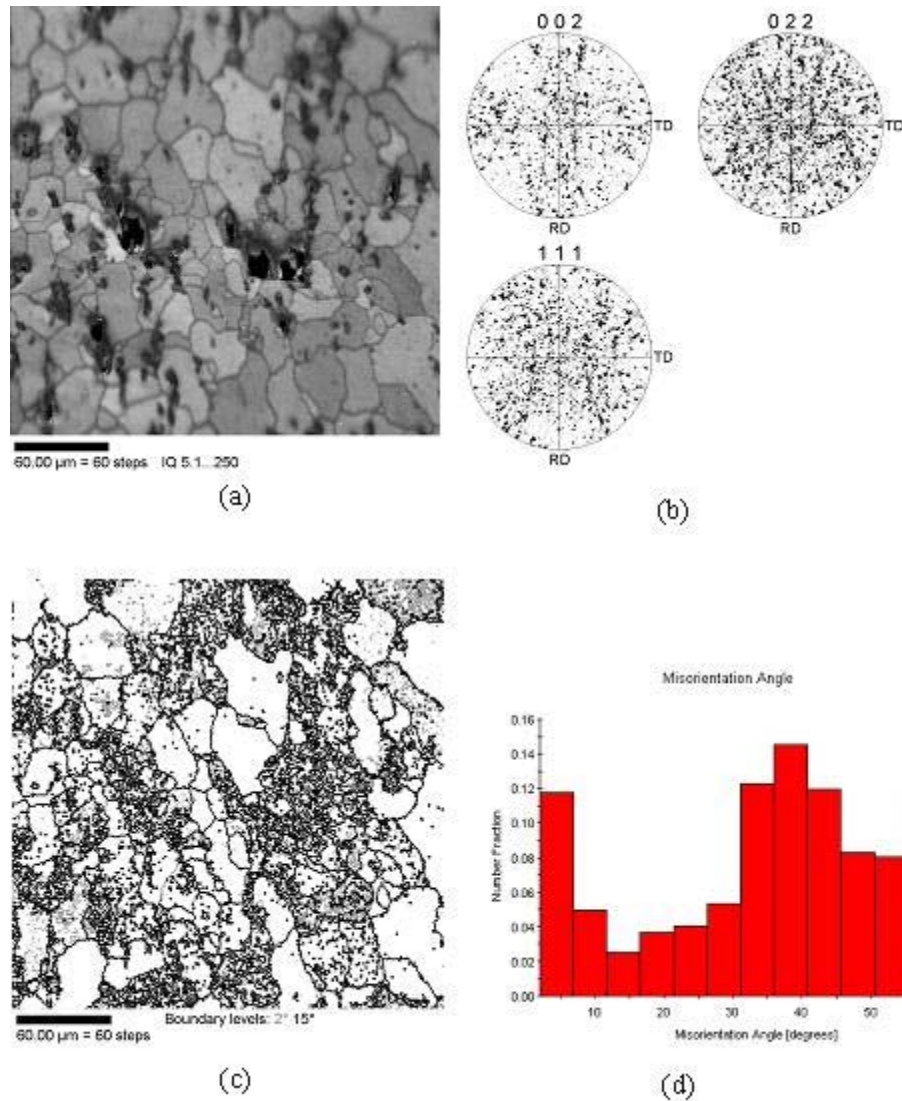
Figure 37. Microstructure and microtexture data for the 978931(K)-2, 450 °C, 1 x 10^{-2} s^{-1}. (a) IQ grayscale map exhibits large, equiaxed microstructure. (b) Pole figures revealing a random microtexture with strong <100> fibers. (c) Grain boundary map outlining the high angle and low angle boundaries. (d) Histogram of disorientation angles reveals the high degree of high angle boundaries associated with the microstructure, as well as, a significant amount of low angle boundaries.
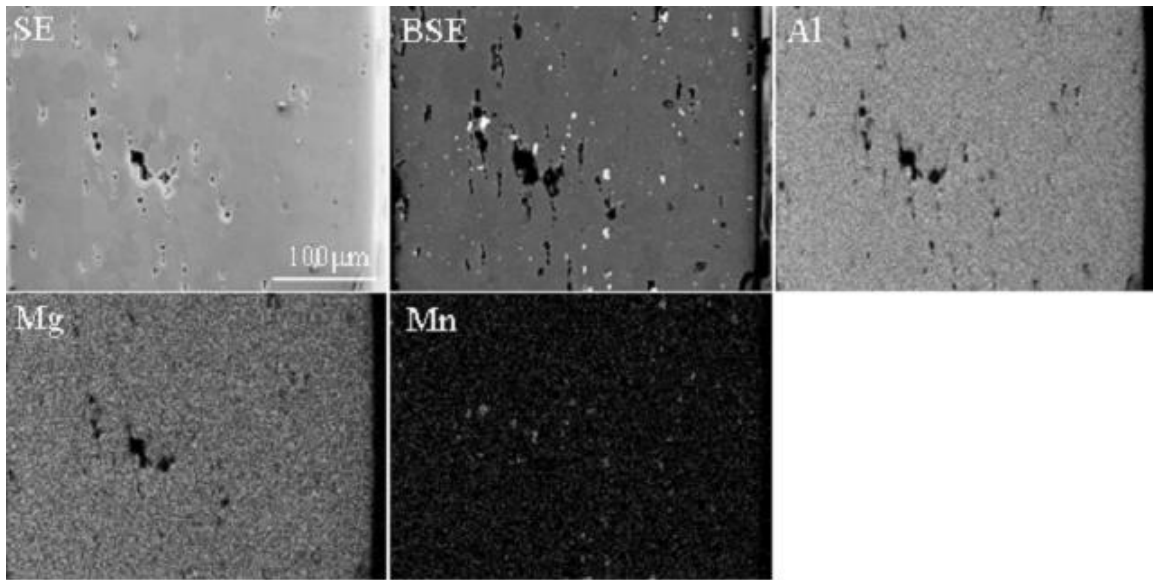
Figure 38. SE, BSE and Al, Mg and Mn X-ray maps of plane strain bulge material 978931(K)-1, 450 °C, 1 x 10^{-2} s^{-1}– dislocation deformation by solute drag creep.

Figure 39. SE, BSE and Al, Mg and Mn X-ray maps of plane strain bulge material 978931(K)-2, 450 °C, 1 x 10^{-2} s^{-1}– dislocation deformation by solute drag creep.

.

Figure 40. Boundaries and cavity formation under plane strain conditions. Plane strain dome test at 450°C, 1×10^{-2} s^{-1}. Histogram showing the distribution of cavities as a function of disorientation angle for the plane strain dome test material 978931(K).
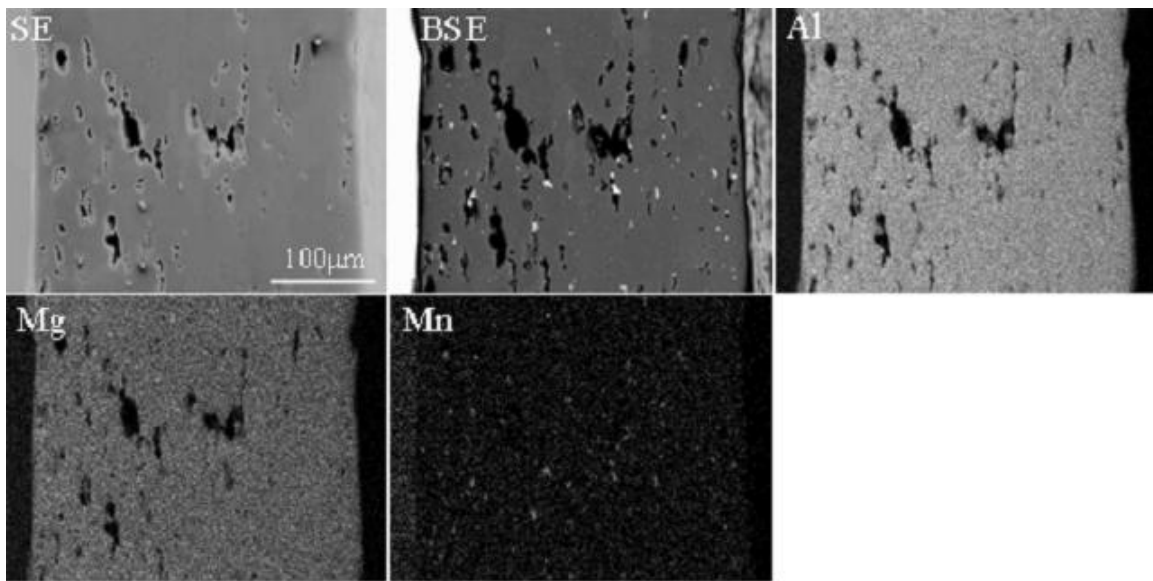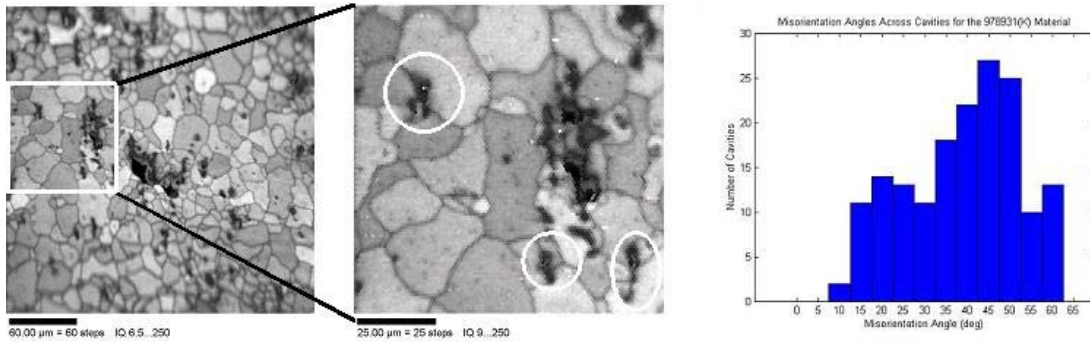
V. CONCLUSION

A. CONCLUSION

1. Transitions apparent in mechanical property data reflect independent contributions of GBS and dislocation creep mechanisms.
   a. GBS is accompanied by randomizing of texture.
   b. Dislocation creep is indicated by formation of fiber texture components.

2. Cavity formation under uniaxial tension occurs by GBS on boundaries of disorientation $> °7$.

3. A disorientation threshold for cavity formation is consistent with pure aluminum data. (Weinberg, Ref. 16)

4. Cavity formation may occur in the apparent absence of particles residing on grain boundaries.

5. Cavities form under biaxial tension by GBS despite deformation under dislocation creep conditions.

6. The sample deformed under nominally plane strain conditions exhibited varying degrees of strain despite having a nominal strain rate of 1×10^{-2} s^{-1}. Again, cavities form under plane strain conditions by GBS despite deformation under creep conditions.

7. Analysis of cavity formation and growth must consider both the formation mechanism (GBS) as well as growth under combined dislocation and GBS processes.

61

B. RECOMMENDATIONS FOR FURTHER STUDY

1. Broaden analysis of cavity formation through transmission electron microscopy (TEM)
   a. To determine distinguishing features of boundaries in materials of varying ductility.
   b. Cavity initiation mechanisms.
   c. And, mechanisms involved in both cavity growth and linkage.

2. Application to components undergoing superplastic forming to determine local deformation mechanisms
   a. Biaxial dome samples representing varying strains for strain rates in both the GBS and dislocation creep regimes.
   b. Plane strain dome samples representing varying strains for strain rates in both the GBS and dislocation creep regimes.

3. Analysis of different portions of the biaxial dome and plane strain bulge regions using combined microscopy techniques to investigate the earlier stages of cavitation.

LIST OF REFERENCES

1. Verma, R., Friedman, P.A., Ghosh, A.K., Kim, C. and Kim, S. "Superplastic Forming Characteristics of Fine-Grained 5083." *J. Mater. Sci. Eng.* Vol. 4(5), pp.543-550, 1995.

2. Nieh, T.G., Wadsworth, J., and Sherby, O.D. *Superplasticity in Metals and Ceramics*. New York: Cambridge University Press, 1997.

3. Hertzberg, R.W. *Deformation and Fracture Mechanics of Engineering Materials.* 4th *ed*. New York: John Wiley & Sons, Inc., 1996.

4. Maestas, T.A., *Study of Processing and Microstructure of a Superplastic 5083 Aluminum Alloy*, Master's Thesis, Naval Postgraduate School, Monterey, CA, March 2002.

5. Harrell, J.W., *Analysis of the Transition in Deformation Mechanisms in Superplastic 5083 Aluminum Alloys by Orientation Imaging Microscopy,* Master's Thesis, Naval Postgraduate School, Monterey, CA, December 2001.

6. Sherby, O.D. and Wadsworth, J., *Deformation Processing and Structure*, p. 355, 1984.

7. Ghosh, A.K., Bae, D.H. and Semiatin, S.L. "Initiation and Early Sages of Cavity Growth during Superplastic and Hot Deformation." *Matls. Sci. Forum .* Vol. 304-306, pp. 609-616, 1999.

8. Khaleel, M.A., Zbib, H.M., and Nyberg, E.A. "Constitutive Modeling of Deformation and Damage in Superplastic Materials." *International J. of Plasticity*. Vol. 17, pp. 277-296, 2001.

9. Taleff, E.M., Lesuer, D.R., Syn, C.K. and Henshall, G.A. "Creep Fracture During Solute-Drag Creep and Superplastic Deformation." Mahidhara, R.K., Getlmacher, A.B., Matic, P. and Sadananda, K. (Ed.) *Recent Advances in Fracture*. The minerals, Metals & Materials Society, 1997.

10. Kulas, M.A., *The Optimization of 5083 Aluminum Alloy Ductilities in Superplastic Forming.* Ph D. Dissertation Research, University of Texas, Austin, TX, September 2002.

11. Beckwith, T.G., Maragoni, R.D. Lienhard V., J.H. *Mechanical Measurements*. 5th ed. New York: Addison-Wesley Publishing Company, Inc., 1993.

12. Smallman, R.E., Bishop, R.J. *Modern Physical Metallurgy and Materials Engineering Sixth Edition*. Oxford: Butterworth-Heinemann, 1999.

13. TexSEM Laboratories, Incorporated. *OIM DC User's Manual*. 3 January 2001.

14. Randle, V. *Microtecture Determination and Its Applications*. The Institute of Metal, 1992.

15. Taleff, E.F. and Kulas, M.A., Private Communications, January 2003.

16. Weinberg, F. "Grain Boundary Shear in Aluminum." *Trans. AIME*. Vol. 212, pp. 808-17, 1958.

17. Perez-Prado, M.T., Gonzalez-Doncel, G., Ruano, O.A. and McNelley, T.R. "Texture Analysis of the Transition from Slip to Grain Boundary Sliding in a Discontinuously Recrystallized Superplastic Aluminum Alloy." *Acta Materialia*. Vol.49, pp. 2259-2268, 2001.

18. Mackenzie, J.K., *Biometrica*, v. 45, p. 229, 1958.

19. Kokawa, H., Tadao, W. and Karashima, S. "Sliding Behavior and Dislocation Structures in Aluminum Grain Boundaries." *Phil. Mag. A.* Vol. 44(6), pp. 1239-1254, 1981

20. Taylor, M.B, Zbib, H.M. and Khaleel, M.A. "Damage and Size Effect during Superplastic Deformation." *Int. J. Plasticity*. pp. 1-28, 30 August 2000.

21. Taleff, E.M. "Nondestructive Evaluation of Cavitation in an Al-Mg Material Deformed Under Creep Conditions." *J. Mater. Res*. Vol. 15(1), p. 76-84, 2000.

22. Khraishi, T.A., Khaleel, M.A. and Zbib, H.M. "A Parametric-Experimental Study of Void Growth in Superplastic Deformation." *International J. of Plasticity*. Vol. 17, pp. 297-315, 2001.

23. Kannan, K. and Hamilton, C.H. "Inhomogeneities in Initial Cavity Distribution in a Superplastic Al 5083 Alloy." *Scripta Mater*. Vol. 38(2), pp. 299-305, 1998.

24. Ghosh, A.K. and Bae, D.H. "Microstructral Effects on Cavitation, Flow Localization and Fracture in Superplastic Metals." *Matls. Sci. Forum*. Vol. 243-245, pp. 89-98, 1997.

25. Stowell, M.J., "Cavitation in Superplasticity." Paton, N.E. and Hamilton, C.H. (Ed.) *Superplastic Forming of Structural Alloys*. pp. 321-336. Warrendale: Metallurical Society of AIME, 1982.

THIS PAGE LEFT INTENTIONALLY BLANK

INITIAL DISTRIBUTION LIST

1. Defense Technical Information Center
    Ft. Belvoir, VA

2. Dudley Knox Library
    Naval Postgraduate School
    Monterey, CA

3. Engineering and Technology Curricular Office, Code 34
    Naval Postgraduate School
    Monterey, CA

4. Department Chairman, Code ME/Mc
    Naval Postgraduate School
    Monterey, CA

5. Professor Terry R. McNelley, Code ME/Mc
    Naval Postgraduate School
    Monterey, CA

6. Professor Eric Taleff
    The University of Texas at Austin
    Austin, TX

7. Dr. Paul E. Krajewski
    General Motors Corp.
    Warren, MI

8. LT. Juanito F. Boydon, Jr.
    Naval Postgraduate School
    Monterey, CA